A high-order cell-centered Lagrangian scheme for compressible fluid flows in two-dimensional cylindrical geometry

Pierre-Henri Maire

UMR CELIA, Université Bordeaux I, 351 Cours de la Libération, 33 405 Talence, France

ARTICLE INFO

ABSTRACT

The goal of this paper is to present high-order cell-centered schemes for solving the equations of Lagrangian gas dynamics written in cylindrical geometry. A node-based discretization of the numerical fluxes is obtained through the computation of the time rate of change of the cell volume. It allows to derive finite volume numerical schemes that are compatible with the geometric conservation law (GCL). Two discretizations of the momentum equations are proposed depending on the form of the discrete gradient operator. The first one corresponds to the control volume scheme while the second one corresponds to the so-called area-weighted scheme. Both formulations share the same discretization for the total energy equation. In both schemes, fluxes are computed using the same nodal solver which can be viewed as a two-dimensional extension of an approximate Riemann solver. The control volume scheme is conservative for momentum, total energy and satisfies a local entropy inequality in its first-order semi-discrete form. However, it does not preserve spherical symmetry. On the other hand, the area-weighted scheme is conservative for total energy and preserves spherical symmetry for one-dimensional spherical flow on equiangular polar grid. The two-dimensional high-order extensions of these two schemes are constructed employing the generalized Riemann problem (GRP) in the acoustic approximation. Many numerical tests are presented in order to assess these new schemes. The results obtained for various representative configurations of one and two-dimensional compressible fluid flows show the robustness and the accuracy of our new schemes.

1. Introduction

This paper deals with high-order cell-centered discretizations of the Lagrangian hydrodynamics equations written in cylindrical geometry. The present discretizations are extensions, in two-dimensional axisymmetric geometry, of the cell-centered Lagrangian schemes described in [24,23]. We note that the high-order extension, which is constructed using the generalized Riemann problem (GRP) methodology of Ben-Artzi and Falcovitz [6], is genuinely two-dimensional. This axisymmetric extension is motivated since in many application problems, such as inertial confinement problems, physical domains have axisymmetric features. In this framework, the importance of preserving spherical symmetry is well recognized, particularly for the numerical simulations of implosions.

A common feature shared by Lagrangian hydrodynamics methods is that computational cells move with the flow velocity. In practice, this means that the cell vertices move with a computed velocity, the cell faces being uniquely specified by the

vertex positions. Thus, Lagrangian methods can capture contact discontinuity sharply in multimaterial fluid flows. However, in the Lagrangian framework, one has to discretize not only the gas dynamics equations but also the vertex motion in order to move the mesh. Moreover, the numerical fluxes of the physical conservation laws must be determined in a compatible way with the vertex velocity so that the geometric conservation law (GCL) is satisfied, namely the rate of change of a Lagrangian volume has to be computed coherently with the node motion. This critical requirement is the cornerstone of any Lagrangian multi-dimensional scheme.

The most natural way to solve this problem employs a staggered discretization in which position, velocity and kinetic energy are centered at points, while density, pressure and internal energy are within cells. The dissipation of kinetic energy into internal energy through shock waves is ensured by an artificial viscosity term. Since the seminal works of von Neumann and Richtmyer [34], and Wilkins [36], many developments have been made in order to improve the accuracy and the robustness of staggered hydrodynamics [12,10,8]. More specifically, the construction of a compatible staggered discretization leads to a scheme that conserves total energy in a rigorous manner [11,9]. Concerning the critical issue related to spherical symmetry preservation many works have been done in the framework of staggered-grid hydrodynamics. The most widely used method that preserves symmetry exactly on polar grids with equi-angular zoning is the area weighted method. In this approach one uses a Cartesian form of the momentum equation in cylindrical coordinates system, hence integration is not performed with respect to the true volume in cylindrical coordinates, but rather with respect to area. However, due to the loss of compatibility between gradient and divergence operators, this formulation, in its usual form, does not allow the conservation of total energy as it has been explained by Whalen [35]. This flaw has been corrected in [11] by constructing a compatible area-weighted scheme which preserves total energy. In [27,28], Margolin and Shashkov use a curvilinear grid to construct conservative symmetry preserving discretizations. Their strategy use high-order curves to connect the nodes, so that planar, cylindrical and spherical symmetry are exactly maintained while differential operators are discretized in a compatible way. It is worth to mention that this method preserves symmetry even on polar mesh with non-equal angles. In [13], Caramana and Whalen show how to achieve the problem of exactly preserving a one-dimensional symmetry, in a two-dimensional coordinate system distinct from that symmetry. This result is attained through a modification of the pressure gradient operator used to compute the force in a staggered-grid hydrodynamics algorithm. Regarding the control volume discretization, a general methodology is described in [26], where a discrete divergence operator is derived by requiring consistency of the divergence of the velocity field with the time rate of change of volume of a cell. The discrete gradient operator is deduced from the discrete divergence using conservation of total energy which implies the adjointness of the discrete gradient and divergence operators.

In this paper, we propose an alternative discretization which can be viewed as a Godunov-type method. Following [15,24], we present a discretization in which all conserved quantities, including momentum, and hence cell velocity are cell-centered. The main feature of this discretization lies in the fact that the interface fluxes and the node velocity are computed coherently thanks to an approximate Riemann solver located at the nodes. Indeed, the rate of change of any Lagrangian volume is computed coherently with the nodes displacement. This unstructured scheme, in two and three-dimensional Cartesian geometry, conserves momentum and total energy [23,25]. It also fulfills a local entropy inequality in its first-order version. Regarding the axisymmetric extension of these Godunov-type schemes, we observe that recent developments have been described in [29,31]. However, we note that these extensions are only first-order discretizations and therefore not sufficiently accurate for real-life applications. It is also worth to mention that a special cell-centered method, which preserves symmetry, has been developed in [33].

Here, we provide high-order discretizations written in Cartesian coordinates devoted to the cylindrical geometry. Two schemes, which are compatible with the GCL, are obtained through the use of a node-based discretization of the numerical fluxes. These two schemes differ in the way the momentum equation is discretized. The first one, which uses a gradient operator compatible with the divergence operator, corresponds to the control volume scheme, while the second one corresponds to the area-weighted scheme. Both formulations share the same discretization for the total energy equation. We note that in both schemes fluxes are computed using the same nodal solver which can be viewed as two-dimensional extension of an approximate Riemann solver. The control volume scheme conserves momentum, total energy and satisfies a local entropy inequality in its first-order semi-discrete form. However, it does not preserves spherical symmetry. On the other hand, the area weighted formulation conserves total energy and preserves spherical symmetry for one-dimensional spherical flow computed on equi-angular polar grid. The genuinely two-dimensional high-order extension of both schemes is constructed utilizing the GRP methodology in its acoustic approximation.

The remainder of this paper is structured as follows: the governing equations of Lagrangian hydrodynamics, written in pseudo Cartesian geometry, are described in Section 2. The first-order discretizations corresponding to the control volume and the area-weighted schemes are derived in Section 3. In this section we also address the problem of symmetry preservation. The acoustic GRP high-order extension of the previous schemes are detailed in Section 4. Criteria for time step limitation are presented in Section 5. Numerical experiments, for both formulations, are reported in Section 6. They show not only the robustness and the accuracy of the present methods but also their abilities to handle successfully complex two-dimensional flows. More specifically, we show that the area-weighted scheme satisfies the requirement of wavefront invariance and is able to compute properly isentropic compression. Concluding remarks and perspectives are given in Section 7.

2. Lagrangian hydrodynamics in 2D pseudo Cartesian geometry

We are interested in discretizing the equations of the Lagrangian hydrodynamics in pseudo Cartesian geometry, taking into account under the same form both Cartesian and cylindrical geometry. To this end, we use the same notations as those introduced by Dukowicz and co-workers in [1].

2.1. Governing equations and notations

In the Lagrangian formalism the rates of change of mass, volume, momentum and total energy are computed assuming that the computational volumes follow the material motion. This leads to the following set of equations for an arbitrary moving control volume V_t

$$\frac{d}{dt}\int_{V_t}\rho\,dV = 0, \tag{1a}$$

$$\frac{d}{dt}\int_{V_t}dV - \int_{V_t}\nabla\cdot\boldsymbol{U}\,dV = 0, \tag{1b}$$

$$\frac{d}{dt}\int_{V_t}\rho\boldsymbol{U}\,dV + \int_{V_t}\nabla P\,dV = \boldsymbol{0}, \tag{1c}$$

$$\frac{d}{dt}\int_{V_t}\rho E\,dV + \int_{V_t}\nabla\cdot P\boldsymbol{U}\,dV = 0, \tag{1d}$$

where $\frac{d}{dt}$ denotes the material, or Lagrangian, time derivative. Here, $\rho, \boldsymbol{U}, P, E$ denote the mass density, velocity, pressure and specific total energy of the fluid. Eqs. (1a), (1c) and (1d) express the conservation of mass, momentum and total energy. The thermodynamical closure of the set of Eq. (1) is obtained by adding the equation of state of the form

$$P = P(\rho, \varepsilon), \tag{2}$$

where the specific internal energy, ε, is related to the specific total energy by $\varepsilon = E - \frac{1}{2}\boldsymbol{U}^2$.

We note that volume variation Eq. (1b), which is also named geometric conservation law (GCL), is equivalent to the local kinematic equation

$$\frac{d\boldsymbol{X}}{dt} = \boldsymbol{U}, \quad \boldsymbol{X}(0) = \boldsymbol{x}, \tag{3}$$

where $\boldsymbol{X}$ is a point located on the control volume surface, $S(t)$, at time $t > 0$ and $\boldsymbol{x}$ corresponds to its initial position.

Let us introduce some notations. First, we note that the case of Cartesian or cylindrical geometry can be combined by introducing the pseudo Cartesian frame (O, X, Y), equipped with the orthonormal basis $(\boldsymbol{e}_X, \boldsymbol{e}_Y)$, through the use of the pseudo radius

$$\mathcal{R}(Y) = 1 - \alpha + \alpha Y,$$

where $\alpha = 1$ for cylindrical geometry and $\alpha = 0$ for Cartesian geometry. We remark that Y corresponds to the radial coordinate in the cylindrical case. This means that we assume rotational symmetry about X axis, refer to Fig. 1. We note that if we refer to standard cylindrical coordinates, (Z, R), then X corresponds to Z and Y to R. In this framework, the volume V is ob-
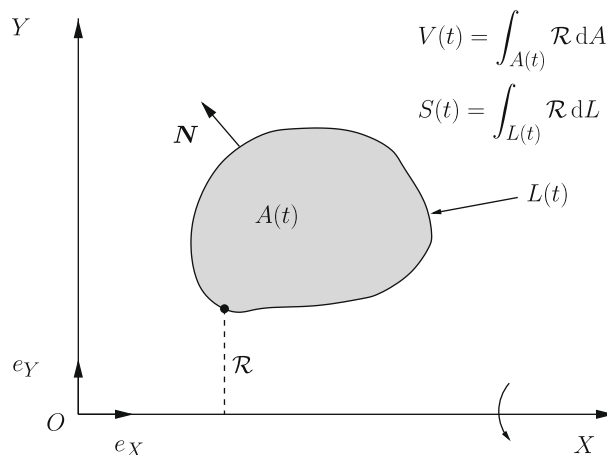

$$V(t) = \int_{A(t)}\mathcal{R}\,dA$$

$$S(t) = \int_{L(t)}\mathcal{R}\,dL$$

Fig. 1. Notations related to the pseudo Cartesian geometry.

tained by rotating the area A about the X axis. Thus, the volume element, dV, writes $dV = \mathcal{R}\,dA$, where $dA = dXdY$ is the area element in the pseudo Cartesian coordinates. Note that we have omitted the factor 2π due to the integration in the azimuthal direction, namely we consider all integrated quantities to be defined per unit radian. The surface S, which bounds the volume V, is obtained by rotating, L, the boundary of the area A, about the X axis. Thus, the surface element, dS, writes $dS = \mathcal{R}\,dL$, where dL is the line element along the perimeter of A.

2.2. Definition of the divergence and the gradient operators

In view of subsequent spatial discretization, we shall express the volume integrals associated with the divergence and gradient operators using the Green formula. We recall that, in the pseudo Cartesian frame, the divergence operator writes

$$\nabla \cdot \boldsymbol{U} = \frac{\partial u}{\partial X} + \frac{1}{\mathcal{R}}\frac{\partial}{\partial Y}(\mathcal{R}v) = \frac{\partial u}{\partial X} + \frac{\partial v}{\partial Y} + \alpha\frac{v}{\mathcal{R}} = \frac{1}{\mathcal{R}}\left[\frac{\partial}{\partial X}(\mathcal{R}u) + \frac{\partial}{\partial Y}(\mathcal{R}v)\right],$$

where u, v are the components of the vector $\boldsymbol{U}$. The gradient operator writes as usual

$$\nabla P = \frac{\partial P}{\partial X}\boldsymbol{e}_X + \frac{\partial P}{\partial Y}\boldsymbol{e}_Y.$$

Let us replace the volume integral form of the divergence operator by its surface integral form, employing the previous notations

$$\int_V \nabla\cdot\boldsymbol{U}\,dV = \int_A \frac{1}{\mathcal{R}}\left[\frac{\partial}{\partial X}(\mathcal{R}u) + \frac{\partial}{\partial Y}(\mathcal{R}v)\right]\mathcal{R}\,dA = \int_A \left[\frac{\partial}{\partial X}(\mathcal{R}u) + \frac{\partial}{\partial Y}(\mathcal{R}v)\right]dA = \int_L \boldsymbol{U}\cdot\boldsymbol{N}\mathcal{R}\,dL,$$

where $\boldsymbol{N}$ is the unit outward normal associated with the contour L. Thus, the Green formula in the pseudo Cartesian framework reads

$$\int_V \nabla\cdot\boldsymbol{U}\,dV = \int_L \boldsymbol{U}\cdot\boldsymbol{N}\mathcal{R}\,dL. \qquad 4$$

To derive the surface integral form of the gradient operator, we use the vectorial identity

$$\boldsymbol{U}\cdot\nabla P = \nabla\cdot P\boldsymbol{U} - P\nabla\cdot\boldsymbol{U},$$

which holds for any vector $\boldsymbol{U}$. The integration of this identity over the volume V, using the previous notations and the above Green formula, leads to

$$\int_V \boldsymbol{U}\cdot\nabla P\,dV = \int_L P\boldsymbol{U}\cdot\boldsymbol{N}\mathcal{R}\,dL - \int_A P\nabla\cdot\boldsymbol{U}\mathcal{R}\,dA.$$

Assuming a constant $\boldsymbol{U}$ vector, we finally get

$$\int_V \nabla P\,dV = \int_L P\boldsymbol{N}\mathcal{R}\,dL - \alpha\boldsymbol{e}_Y \int_A P\,dA, \qquad 5$$

since for a constant $\boldsymbol{U}$ vector, we have $\nabla\cdot\boldsymbol{U} = \frac{\alpha}{\mathcal{R}}\boldsymbol{U}\cdot\boldsymbol{e}_Y$. We have expressed the volume integral of the gradient operator as a function of a surface integral plus a source term, using a vectorial identity, which ensures the compatibility with the surface integral form of the divergence operator. This approach leads to a discretization which is known as *control volume formulation*. An alternative approach to define the surface integral form of the gradient operator is obtained by setting

$$\int_V \nabla P\,dV = \int_A \nabla P\mathcal{R}\,dA = \overline{\mathcal{R}}\int_A \nabla P\,dA.$$

Here, we have used the mean value theorem, hence $\overline{\mathcal{R}}$ is defined as the averaged pseudo radius

$$\overline{\mathcal{R}} = \frac{1}{A}\int_A \mathcal{R}\,dA, \qquad 6$$

where $A = \int_A dA$ is the surface of the area A. We remark that in the case of Cartesian geometry $\overline{\mathcal{R}} = 1$ since $\alpha = 0$. Finally, applying the Green formula once again, we get

$$\int_V \nabla P\,dV = \overline{\mathcal{R}}\int_L P\boldsymbol{N}\,dL. \qquad 7$$

We recover the Cartesian definition of the gradient operator weighted by the averaged pseudo radius. This alternative approach leads to the so-called *area-weighted formulation*. We point out that, in this case, the compatibility between the surface integrals of the divergence and gradient operators has been lost. Let us note that formulae (7) and (5) coincide in the case of the Cartesian geometry since $\alpha = 0$ and $\overline{\mathcal{R}} = 1$.

In what follows, we shall derive and thoroughly analyze the discrete schemes deduced from the control volume and the area weighted formulations.

Comment 1. We remark that if the scalar P is constant over the volume V, then Eq. (5) yields the following geometric identity

$$\int_L \boldsymbol{N} \mathcal{R} \, dL = \alpha A \, \boldsymbol{e}_Y, \tag{8}$$

which can also be written component-wise

$$\int_L N_X \mathcal{R} \, dL = 0,$$
$$\int_L N_Y \mathcal{R} \, dL = \alpha A,$$

where N_X, N_Y are the components of the N unit outward vector. For $\alpha = 0$, we recover the well known result, that for a closed contour, the integral of the normal over this contour is equal to zero. Note that this result does not hold anymore in the case of cylindrical geometry.

2.3. Control volume formulation

Using the previous results and particularly the gradient operator defined by Eq. (5), we rewrite the set of Eq. (1) in a control volume formulation

$$m \frac{d}{dt} \left\langle \frac{1}{\rho} \right\rangle - \int_L \boldsymbol{U} \cdot \boldsymbol{N} \mathcal{R} \, dL = 0, \tag{9a}$$

$$m \frac{d}{dt} \langle \boldsymbol{U} \rangle + \int_L P \boldsymbol{N} \mathcal{R} \, dL - \alpha \boldsymbol{e}_Y \int_A P \, dA = \boldsymbol{0}, \tag{9b}$$

$$m \frac{d}{dt} \langle E \rangle + \int_L P \boldsymbol{U} \cdot \boldsymbol{N} \mathcal{R} \, dL = 0. \tag{9c}$$

Here, $m = \int_V \rho \, dV$ denotes the mass of the volume V, which is constant according to Eq. (1a). For any fluid variable ϕ, $\langle \phi \rangle$ denotes its mass density average, i.e.

$$\langle \phi \rangle = \frac{1}{m} \int_V \rho \phi \, dV.$$

Introducing $V = \int_A \mathcal{R} \, dA$ the measure of the volume V, Eq. (9a) is rewritten as a geometric conservation law:

$$\frac{d}{dt} V - \int_L \boldsymbol{U} \cdot \boldsymbol{N} \mathcal{R} \, dL = 0. \tag{10}$$

Using the identity (8) derived in Comment 1, we rewrite the source term in the momentum equation as a flux term and get

$$m \frac{d}{dt} \langle \boldsymbol{U} \rangle + \int_L \left(P - \overline{P} \right) \boldsymbol{N} \mathcal{R} \, dL = \boldsymbol{0}, \tag{11}$$

where $\overline{P}$ denotes the surface averaged pressure defined as follows

$$\overline{P} = \frac{1}{A} \int_A P \, dA.$$

The set of the previous equations will be used in the subsequent sections in order to derive the control volume discretization.

2.4. Area-weighted formulation

The area-weighted formulation is obtained through the use of identity (7) for the gradient operator definition. In comparison to the control volume formulation, it differs only in the momentum equation. Using the notations previously introduced, the area weighted formulation of the momentum equation writes

$$m \frac{d}{dt} \langle \boldsymbol{U} \rangle + \overline{\mathcal{R}} \int_L P \boldsymbol{N} \, dL = \boldsymbol{0}, \tag{12}$$

where the averaged pseudo radius has been defined in (6). We point out that, in the case of Cartesian geometry $\overline{\mathcal{R}} = 1$, the area weighted formulation coincides with the control volume formulation.

Knowing that $m = V \langle \frac{1}{\rho} \rangle^{-1}$ and $\overline{\mathcal{R}} = \frac{V}{A}$, the momentum Eq. (12) can be rewritten

$$\mu \frac{d}{dt} \langle \boldsymbol{U} \rangle + \int_L P \boldsymbol{N} \, dL = \boldsymbol{0}, \tag{13}$$

where $\mu = A \langle \frac{1}{\rho} \rangle^{-1}$ denotes the Cartesian inertia. Thus, Eq. (13) can be viewed as a momentum equation written in Cartesian geometry. We note that the Cartesian inertia is not a Lagrangian mass (e.g. it is not constant as time evolves).

3. First-order spatial discretization

The aim of this section is to establish the first-order spatial discretization of the Lagrangian hydrodynamics equations in pseudo Cartesian geometry. To this end, we introduce a node-based discretization of the face fluxes which is compatible with the GCL. According to the choice that is made for the discrete gradient operator, we construct a control volume and an area weighted discretization. We investigate for both discretizations the important problem corresponding to symmetry preservation. Finally, we construct a nodal solver which equally applies for both formulations.

3.1. Notations and assumptions

Let us consider a physical domain $V(t)$ that is filled with the fluid at time t. We assume that we can map $V(t)$ by a set of polygonal cells without gaps or overlaps. Each cell is assigned a unique index c, and is denoted by $\Omega_c(t)$. Each vertex of the mesh is assigned a unique index p and we denote by $\mathcal{P}(c)$ the counterclockwise ordered list of vertices of the cell $\Omega_c(t)$.

3.2. Face flux discretization for the polygonal cell $\Omega_c(t)$

3.2.1. Face flux discretization associated with the control volume formulation
To get the discrete evolution equations for the primary variables $\left(\frac{1}{\rho}, \boldsymbol{U}, E\right)$, we apply the control volume formulation (9) to the polygonal cell $\Omega_c(t)$, which has been rotated about X axis (refer to Fig. 2). Let m_c denotes the constant mass of this cell. We introduce for each flow variable ϕ, its mass-averaged value defined by

$$\phi_c = \frac{1}{m_c} \int_{\Omega_c(t)} \rho \phi \, \mathrm{d}V,$$

then system (9) writes

$$m_c \frac{d}{dt} \left(\frac{1}{\rho_c} \right) - \sum_{f \in \mathcal{F}(c)} \mathcal{R}_f^c L_f^c \boldsymbol{U}_f^c \cdot \boldsymbol{N}_f^c = 0, \tag{14a}$$

$$m_c \frac{d}{dt} \boldsymbol{U}_c + \sum_{f \in \mathcal{F}(c)} \mathcal{R}_f^c L_f^c \Pi_f^c \boldsymbol{N}_f^c - \alpha A_c P_c \boldsymbol{e}_Y = \boldsymbol{0}, \tag{14b}$$

$$m_c \frac{d}{dt} E_c + \sum_{f \in \mathcal{F}(c)} \mathcal{R}_f^c L_f^c \left(\Pi \boldsymbol{U} \right)_f^c \cdot \boldsymbol{N}_f^c = 0. \tag{14c}$$

Here, we have used the index f to denote a generic face of the cell Ω_c whose vertices are point p and p^+, refer to Fig. 2. L_f^c denotes the length of this face, $\mathcal{R}_f^c = \frac{1}{2}(\mathcal{R}_p + \mathcal{R}_{p^+})$ is the pseudo radius of its midpoint and $\boldsymbol{N}_f^c$ its unit outward normal. We remark that the product $\mathcal{R}_f^c L_f^c$ is nothing but the surface generated by the rotation of the face f about X axis. We have also
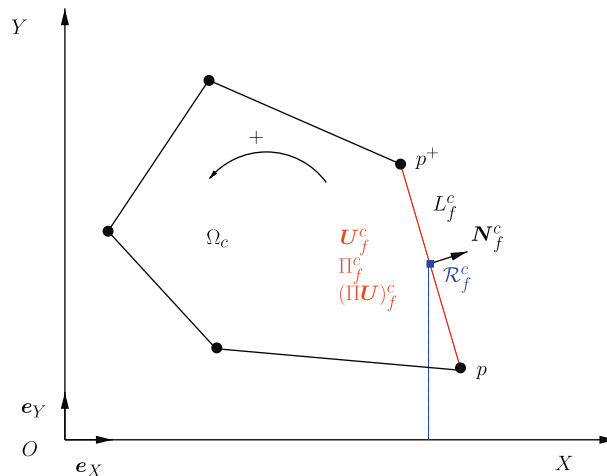

Fig. 2. Notations related to the polygonal cell $\Omega_c(t)$.

introduced the set $\mathcal{F}_c$, which is the set of the faces of cell Ω_c. In the source term of the momentum equation A_c stands for the surface of the polygonal cell Ω_c. The face fluxes $\boldsymbol{U}_f^c, \Pi_f^c, \ \Pi\boldsymbol{U}_f^c$ are defined as follows

$$\boldsymbol{U}_f^c \quad \frac{1}{\mathcal{R}_f^c L_f^c} \int_f \boldsymbol{U}\mathcal{R}\,dL, \tag{15a}$$

$$\Pi_f^c \quad \frac{1}{\mathcal{R}_f^c L_f^c} \int_f P\mathcal{R}\,dL, \tag{15b}$$

$$\Pi\boldsymbol{U}_f^c \quad \frac{1}{\mathcal{R}_f^c L_f^c} \int_f P\boldsymbol{U}\mathcal{R}\,dL. \tag{15c}$$

Using the previous notations, the geometric identity (8) writes under the discrete form

$$\sum_{f\in\mathcal{F}_c} \mathcal{R}_f^c L_f^c \boldsymbol{N}_f^c \quad \alpha A_c \boldsymbol{e}_Y. \tag{16}$$

With the help of this discrete geometric identity, we rewrite the momentum equation transforming the source term into a flux term

$$m_c \frac{d}{dt}\boldsymbol{U}_c \quad \sum_{f\in\mathcal{F}_c} \mathcal{R}_f^c L_f^c \ \Pi_f^c \quad P_c \ \boldsymbol{N}_f^c \quad \boldsymbol{0}. \tag{17}$$

The local kinematic equation in its discrete form at point p is written

$$\frac{d}{dt}\boldsymbol{X}_p \quad \boldsymbol{U}_p, \quad \boldsymbol{X}_p\,0 \quad \boldsymbol{x}_p, \tag{18}$$

where $\boldsymbol{X}_p \quad X_p, Y_p^{\ t}$ denotes the position of point p at time $t > 0$, $\boldsymbol{x}_p$ being its initial position and $\boldsymbol{U}_p$ its velocity.

3.2.2. Face flux discretization associated with the area-weighted formulation

In the case of the area-weighted formulation, we discretize momentum equation using Eq. (12) which has been derived in the previous section and get

$$m_c \frac{d}{dt}\boldsymbol{U}_c \quad \overline{\mathcal{R}}_c \sum_{f\in\mathcal{F}_c} L_f^c \widehat{\Pi}_f^c \boldsymbol{N}_f^c \quad \boldsymbol{0}. \tag{19}$$

Here, $\overline{\mathcal{R}}_c$ denotes the cell-averaged pseudo radius, defined using (6) by $\overline{\mathcal{R}}_c \quad \frac{V_c}{A_c}$, where V_c stands for the volume of the cell Ω_c rotated about X axis. The pressure flux, $\widehat{\Pi}_f^c$, corresponding to the area weighted formulation writes

$$\widehat{\Pi}_f^c \quad \frac{1}{L_f^c} \int_f P\,dL. \tag{20}$$

We point out that its definition quite differs from that of the pressure flux originating from the control volume formulation, previously given in (15b).

Introducing $m_c \quad \rho_c V_c$ and $V_c \quad \overline{\mathcal{R}}_c A_c$ in the momentum Eq. (19), we rewrite it

$$\mu_c \frac{d}{dt}\boldsymbol{U}_c \quad \sum_{f\in\mathcal{F}_c} L_f^c \widehat{\Pi}_f^c \boldsymbol{N}_f^c \quad \boldsymbol{0}, \tag{21}$$

where $\mu_c \quad \rho_c A_c$ stands for the Cartesian inertia. We remark that the discrete area-weighted momentum equation is nothing but the discrete momentum equation written in Cartesian geometry. However, in the case of cylindrical geometry, we note that the Cartesian inertia is not a Lagrangian quantity, e.g. it is not constant during time.

3.2.3. Motivations related to the face flux discretization

System (14) represents the face flux discretization of the Lagrangian hydrodynamics equations, issued from the control volume formulation, for the discrete variables $\left(\frac{1}{\rho_c}, \boldsymbol{U}_c, E_c\right)$. In order to compute the time evolution of the flow variables, we need to calculate the face fluxes $\boldsymbol{U}_f^c, \Pi_f^c$ and $\Pi\boldsymbol{U}_f^c$. We also provided the face flux discretization originating from the area weighted formulation. In this case the time evolution of the flow variables is governed by Eqs. (14a), (19) and (14c). Thus, the evaluation of the face fluxes $\boldsymbol{U}_f^c, \widehat{\Pi}_f^c$ and $\Pi\boldsymbol{U}_f^c$ is needed. In what follows, we shall study thoroughly both discretizations from the point of view of symmetry preservation. More precisely, we will show why the control volume discretization does not preserve spherical symmetry whereas the area weighted discretization ensures it. This important problem will be studied considering a one-dimensional spherical flow computed on an equi-angular polar grid.

Let us remark that, for both formulations, the knowledge of the point velocity $\boldsymbol{U}_p$ is required in order to move the mesh. Moreover, we point out that Eq. (14a) is not only a physical conservation law but also a geometrical conservation law, since $\frac{m_c}{\rho_c} \quad V_c$. Hence, the face flux $\boldsymbol{U}_f^c$ associated with this equation must be computed in a coherent manner with the point velocity $\boldsymbol{U}_p$ so that the volume variation remains coherent with the point motion. This critical requirement must be fulfilled in order

to ensure that the GCL is properly satisfied. In Section 3.4, we will address this problem defining a compatible discrete divergence operator and expressing the face flux $\boldsymbol{U}_f^c$ in terms of the point velocity $\boldsymbol{U}_p$.

3.3. The issue of symmetry preservation

The aim of this section is to compare the control volume formulation and the area-weighted formulation regarding the issue of symmetry preservation. More precisely, we address the problem of preserving spherical symmetry in two-dimensional cylindrical geometry. Being given a one-dimensional spherical flow on a polar grid, equally spaced in angle, we analyze the ability of the discrete gradient operator to maintain spherical symmetry. Using the previous notations, the discrete gradient operator over the cell Ω_c writes

$$\langle \boldsymbol{\nabla}P \rangle_c^{\text{CV}} = \frac{1}{V_c} \sum_{f \in \mathcal{F}_c} \mathcal{R}_f^c L_f^c \left(\Pi_f^c - P_c \right) \boldsymbol{N}_f^c, \quad \text{for the control volume formulation,} \tag{22a}$$

$$\langle \boldsymbol{\nabla}P \rangle_c^{\text{AW}} = \frac{\overline{\mathcal{R}}_c}{V_c} \sum_{f \in \mathcal{F}_c} L_f^c \widehat{\Pi}_f^c \boldsymbol{N}_f^c, \quad \text{for the area-weighted formulation,} \tag{22b}$$

where the face fluxes, Π_f^c and $\widehat{\Pi}_f^c$, are defined according to (15b) and (20). The quadrangular cell Ω_c is surrounded by the four cells $\Omega_b, \Omega_r, \Omega_t, \Omega_l$, the indices corresponding to the bottom, right, top and left positions. The equal angle polar grid, displayed in Fig. 3, is characterized by the angle $\Delta\theta$. The quantities associated with a face shared by the cells Ω_c and Ω_d are denoted by the double subscript index c, d for $d = b, r, t, l$. Since velocity field is radial, in each cell Ω_c the cell-centered velocity is written $\boldsymbol{U}_c = U_c \boldsymbol{e}_c$, where $\boldsymbol{e}_c$ denotes the radial outward unit vector defined at the center of the cell and U_c is the magnitude of the velocity. Due to the spherical symmetry of the flow, the thermodynamical quantities and the velocity magnitude associated with the cells Ω_b, Ω_c and Ω_t are equal.

Now, to achieve the definition of the discrete gradient operators, we compute the face fluxes, Π_f^c and $\widehat{\Pi}_f^c$, using an approximate Riemann problem, which is defined at the cell face. Let us consider the cell face, $f = (c, d)$, shared by the cells Ω_c and Ω_d. The corresponding Riemann problem is defined by the two states $(\rho_c, \boldsymbol{U}_c, P_c)$ and $(\rho_d, \boldsymbol{U}_d, P_d)$ which are located on either side of the face. The solution of the Riemann problem provides the unique pressure $P_{c,d}^\star$ and normal velocity $\mathcal{V}_{c,d}^\star$ of the face. Using the acoustic approximation, one gets

$$P_{c,d}^\star = \frac{Z_d P_c + Z_c P_d}{Z_c + Z_d} + \frac{Z_c Z_d}{Z_c + Z_d} \left(\boldsymbol{U}_d - \boldsymbol{U}_c \right) \cdot \boldsymbol{N}_{c,d}^c,$$

$$\mathcal{V}_{c,d}^\star = \frac{Z_c \boldsymbol{U}_c + Z_d \boldsymbol{U}_d) \cdot \boldsymbol{N}_{c,d}^c}{Z_c + Z_d} + \frac{P_d - P_c}{Z_c + Z_d},$$

where $\boldsymbol{N}_{c,d}^c$ denotes the unit outward normal related to the cell Ω_c and the face (c, d), and Z_c is the acoustic impedance of the cell Ω_c, i.e. the density times the isentropic sound speed. Since $P_{c,d}^\star$ is constant over the face, we get immediately $\Pi_{c,d}^c = \widehat{\Pi}_{c,d}^c = P_{c,d}^\star$. Using the previous assumptions, elementary geometric computations lead to the following expressions for the face fluxes in the angular direction

$$P_{c,b}^\star = P_{c,t}^\star = P_c - Z_c U_c \sin\left(\frac{\Delta\theta}{2}\right). \tag{23}$$
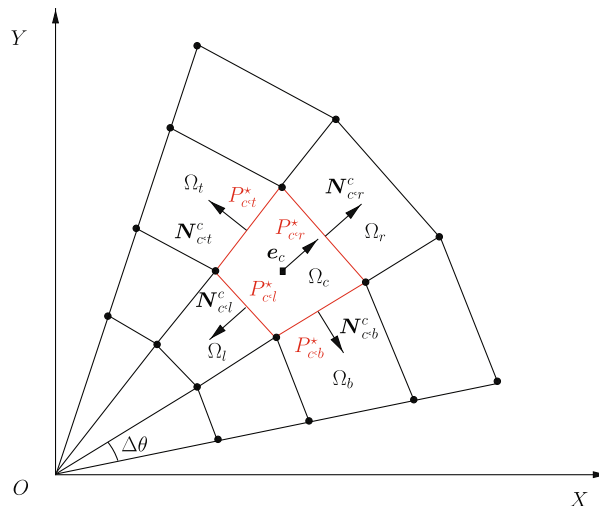

Fig. 3. Equal angle polar grid.

We point out the discrepancy with the constant pressure P_c due to the direction of the cell-centered velocity. The face fluxes in the radial direction writes

$$P_{c,r}^\star \quad \frac{Z_r P_c \quad Z_c P_r}{Z_c \quad Z_r} \quad \frac{Z_c Z_r}{Z_c \quad Z_r} \; U_r \quad U_c \; ,$$

$$P_{c,l}^\star \quad \frac{Z_c P_l \quad Z_l P_c}{Z_l \quad Z_c} \quad \frac{Z_l Z_c}{Z_l \quad Z_c} \; U_c \quad U_l \; .$$

In the case of the control volume formulation, substituting the previous expressions of the face fluxes in (22a) we get

$$V_c \langle \boldsymbol{\nabla} P \, \substack{CV \\ c} \quad \Big[\mathcal{R}_{c,r}^c L_{c,r}^c \Big(P_{c,r}^\star \quad P_c \Big) \quad \mathcal{R}_{c,l}^c L_{c,l}^c \Big(P_{c,l}^\star \quad P_c \Big) \Big] \boldsymbol{e}_c \quad \Big(P_{c,t}^\star \quad P_c \Big) \Big(\mathcal{R}_{c,b}^c L_{c,b}^c \boldsymbol{N}_{c,b}^c \quad \mathcal{R}_{c,t}^c L_{c,t}^c \boldsymbol{N}_{c,t}^c \Big).$$

The first term in the right-hand side, which corresponds to the contribution of the face fluxes in the radial direction, is clearly radial. The second one, which corresponds to the contribution of the face fluxes in the angular direction, is not radial since $P_{c,t}^\star \quad P_c \neq 0$, according to Eq. (23), hence it is responsible for the loss of symmetry. Therefore, the control volume formulation is not able to preserve symmetry. This shortcoming could be addressed by modifying slightly the left and the right states of the Riemann problem at each face. Namely, it is sufficient to replace the cell-centered velocities on both sides of the face by their corresponding interpolated values in angle, at the midpoint of the face. In this way, the viscous part of the interface pressure cancels, which implies $P_{c,b}^\star \quad P_{c,t}^\star \quad P_c$. Therefore, using this modification, the symmetry preservation can be ensured on equi-angular polar grid. We note that similar observation can be found in [7].

In the case of the area-weighted formulation, using the previous results, the discrete gradient operator over the cell Ω_c writes

$$\langle \boldsymbol{\nabla} P \, \substack{AW \\ c} \quad \frac{\overline{\mathcal{R}}_c}{V_c} \Big[\Big(L_{c,r}^c P_{c,r}^\star \quad L_{c,l}^c P_{c,l}^\star \Big) \boldsymbol{e}_c \quad L_{c,t}^c P_{c,t}^\star \boldsymbol{N}_{c,t}^c \quad L_{c,b}^c P_{c,b}^\star \boldsymbol{N}_{c,b}^c \Big].$$

Recalling that the face fluxes in the angular direction are equal and knowing that $L_{c,t}^c \boldsymbol{N}_{c,t}^c \quad L_{c,b}^c \boldsymbol{N}_{c,b}^c \quad \Big(L_{c,r}^c \quad L_{c,l}^c \Big) \boldsymbol{e}_c$, it is clear that the gradient operator is colinear to the radial vector $\boldsymbol{e}_c$, thus leading to symmetry preservation for the area weighted discretization.

3.4. Compatible discretization of the GCL

Knowing that $\frac{m_c}{\rho_c} \quad V_c$, Eq. (14a) is rewritten

$$\frac{dV_c}{dt} \quad \sum_{f \in \mathcal{F} \, c} \mathcal{R}_f^c L_f^c \boldsymbol{U}_f^c \cdot \boldsymbol{N}_f^c \quad 0.$$

The volume of the cell Ω_c, V_c, is a function of the coordinates $\boldsymbol{X}_p$ of point p for $p \in \mathcal{P} \; c$. We compute this volume performing the triangular decomposition displayed in Fig. 4. That is, using the Guldin theorem, we compute the summation of the volumes obtained by rotating the triangle O, p, p about X axis, and we finally get

$$V_c \quad \frac{1}{2} \sum_{p \in \mathcal{P} \, c} \frac{1}{3} \big(\mathcal{R}_O \quad \mathcal{R}_p \quad \mathcal{R}_p \; \big) \; \boldsymbol{X}_p \times \boldsymbol{X}_p \quad \cdot \boldsymbol{e}_Z, \tag{24}$$

where $\boldsymbol{e}_Z \quad \boldsymbol{e}_X \times \boldsymbol{e}_Y$. Note that $\mathcal{R}_O$ denotes the pseudo radius corresponding to the origin, which is defined by $\mathcal{R}_O \quad 1$ for Cartesian geometry and $\mathcal{R}_O \quad 0$ for cylindrical geometry. Following Whalen [35], we time differentiate the volume and after some rearrangements we obtain

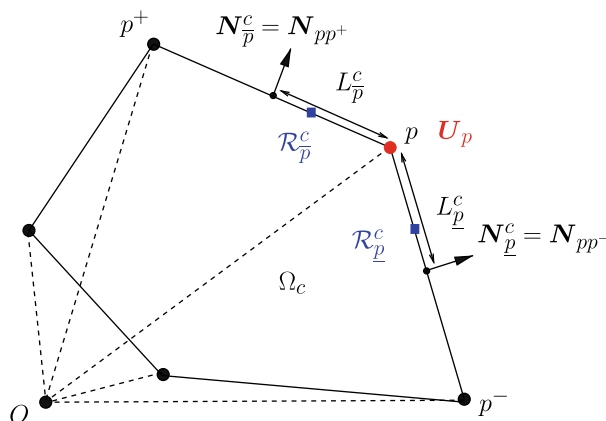**Fig. 4.** Triangular decomposition of the polygonal cell Ω_c.

$$\frac{d}{dt}V_c = \frac{1}{2}\sum_{p\in\mathcal{P}_c}\left(\frac{\mathcal{R}_{p^-}+2\mathcal{R}_p}{3}L_{pp^-}\,\boldsymbol{N}_{pp^-}+\frac{\mathcal{R}_{p^+}+2\mathcal{R}_p}{3}L_{pp^+}\,\boldsymbol{N}_{pp^+}\right)\cdot\boldsymbol{U}_p,$$

where L_{pp^-},L_{pp^+} are the lengths of the edges $[p^-,p]$, $[p,p^+]$ and $\boldsymbol{N}_{pp^-},\boldsymbol{N}_{pp^+}$ are the corresponding unit outward normals. Shifting indices in the summation, the previous equation becomes

$$\frac{d}{dt}V_c = \frac{1}{2}\sum_{p\in\mathcal{P}_c}\left(\frac{\mathcal{R}_{p^-}+2\mathcal{R}_p}{3}\boldsymbol{U}_{p^-}+\frac{\mathcal{R}_{p^+}+2\mathcal{R}_p}{3}\boldsymbol{U}_{p^+}\right)\cdot L_{pp^+}\,\boldsymbol{N}_{pp^+}. \tag{25}$$

The comparison of this equation to the one resulting from the face flux discretization, refer to (14a), shows that they are equivalent provided that the face velocity, $\boldsymbol{U}_f^c$, corresponding to the edge $[p,p^+]$ is written

$$\mathcal{R}_f^c\boldsymbol{U}_f^c = \frac{1}{2}\left(\frac{2\mathcal{R}_p+\mathcal{R}_{p^+}}{3}\boldsymbol{U}_p+\frac{\mathcal{R}_p+2\mathcal{R}_{p^+}}{3}\boldsymbol{U}_{p^+}\right). \tag{26}$$

Here, we have used the fact that $L_{pp^+}=L_f^c$, $\boldsymbol{N}_{pp^+}=\boldsymbol{N}_f^c$ and $\mathcal{R}_f^c=\frac{1}{2}(\mathcal{R}_p+\mathcal{R}_{p^+})$. We remark that this condition could have been obtained computing the integral (15a) expressing the velocity field along the edge with the help of a linear interpolation. Now, we can conclude that the most obvious way to satisfy the compatibility condition (26) consists in first computing the point velocity $\boldsymbol{U}_p$, then deducing the face velocity $\boldsymbol{U}_f^c$. Proceeding in this manner, the compatibility of the face discretization of the geometric conservation law with the time rate of change of the cell volume is always ensured.

Let us introduce some specific notations which shall be used throughout the present paper. To describe the half lengths and the unit outward normals which originate from point p, we set

$$L_{\underline{p}}^c = \frac{1}{2}L_{pp^-},\quad L_{\overline{p}}^c = \frac{1}{2}L_{pp^+},$$
$$\boldsymbol{N}_{\underline{p}}^c = \boldsymbol{N}_{pp^-},\quad \boldsymbol{N}_{\overline{p}}^c = \boldsymbol{N}_{pp^+}.$$

We also define the pseudo radii $\mathcal{R}_{\underline{p}}^c$ and $\mathcal{R}_{\overline{p}}^c$ which are written

$$\mathcal{R}_{\underline{p}}^c = \frac{1}{3}(2\mathcal{R}_p+\mathcal{R}_{p^-}),\quad \mathcal{R}_{\overline{p}}^c = \frac{1}{3}(2\mathcal{R}_p+\mathcal{R}_{p^+}).$$

With the help of these notations, the GCL is rewritten in the following form

$$\frac{d}{dt}V_c = \sum_{p\in\mathcal{P}_c}\left(\mathcal{R}_{\underline{p}}^c L_{\underline{p}}^c\boldsymbol{N}_{\underline{p}}^c+\mathcal{R}_{\overline{p}}^c L_{\overline{p}}^c\boldsymbol{N}_{\overline{p}}^c\right)\cdot\boldsymbol{U}_p. \tag{27}$$

Finally, we employ the previous results to derive the discrete divergence operator over the cell Ω_c

$$\langle\nabla\cdot\boldsymbol{U}\rangle_c = \frac{1}{V_c}\frac{dV_c}{dt} = \frac{1}{V_c}\sum_{p\in\mathcal{P}_c}\left(\mathcal{R}_{\underline{p}}^c L_{\underline{p}}^c\boldsymbol{N}_{\underline{p}}^c+\mathcal{R}_{\overline{p}}^c L_{\overline{p}}^c\boldsymbol{N}_{\overline{p}}^c\right)\cdot\boldsymbol{U}_p. \tag{28}$$

As it has been noticed in [35], the geometric vector between parenthesis, which is called the node area vector, can be identified with the differential of the cell volume with respect to the node position vector. We also point out that, using this node area vector, we can recover another form of the geometric identity (8), which shall be used in what follows

$$\sum_{p\in\mathcal{P}_c}\left(\mathcal{R}_{\underline{p}}^c L_{\underline{p}}^c\boldsymbol{N}_{\underline{p}}^c+\mathcal{R}_{\overline{p}}^c L_{\overline{p}}^c\boldsymbol{N}_{\overline{p}}^c\right) = \alpha A_c\boldsymbol{e}_Y. \tag{29}$$

This formula coincides with Eq. (16) since

$$\sum_{p\in\mathcal{P}_c}\left(\mathcal{R}_{\underline{p}}^c L_{\underline{p}}^c\boldsymbol{N}_{\underline{p}}^c+\mathcal{R}_{\overline{p}}^c L_{\overline{p}}^c\boldsymbol{N}_{\overline{p}}^c\right) = \frac{1}{6}\sum_{p\in\mathcal{P}_c}\left[(2\mathcal{R}_p+\mathcal{R}_{p^-})L_{pp^-}\,\boldsymbol{N}_{pp^-}+(2\mathcal{R}_p+\mathcal{R}_{p^+})L_{pp^+}\,\boldsymbol{N}_{pp^+}\right]$$
$$= \frac{1}{6}\sum_{p\in\mathcal{P}_c}\left[(2\mathcal{R}_p+\mathcal{R}_{p^+})L_{pp^+}\,\boldsymbol{N}_{pp^+}+(2\mathcal{R}_{p^+}+\mathcal{R}_p)L_{pp^+}\,\boldsymbol{N}_{pp^+}\right] = \frac{1}{2}\sum_{p\in\mathcal{P}_c}(\mathcal{R}_p+\mathcal{R}_{p^+})L_{pp^+}\,\boldsymbol{N}_{pp^+}$$
$$= \sum_{f\in\mathcal{F}_c}\mathcal{R}_f^c L_f^c\boldsymbol{N}_f^c.$$

Here, we have shifted the indices in the following way: $p^-\to p$ and $p\to p^+$.

3.5. Node-based discretization of the momentum equation

In this section we present the discretization of the momentum equation for the control volume and the area weighted formulations. This discretization is obtained through the use of the discrete gradient operator associated with each formulation. The discrete gradient operators over the cell Ω_c are constructed introducing two nodal pressures at each node p of the

cell Ω_c. These pressures are denoted $\Pi_{\underline{p}}^c$ and $\Pi_{\overline{p}}^c$, see Fig. 5, they can be seen as nodal pressures viewed from cell Ω_c and related to the two edges impinging at node p.

3.5.1. Control volume formulation

In the case of the control volume formulation, the discrete gradient operator is derived in a compatible manner using the discrete divergence operator defined by Eq. (28). Hence, employing the nodal pressures $\Pi_{\underline{p}}^c$ and $\Pi_{\overline{p}}^c$, the discrete gradient operator writes

$$\langle \nabla P \rangle_c^{\mathrm{CV}} = \frac{1}{V_c} \left[\sum_{p \in \mathcal{P}_c} \left(\mathcal{R}_{\underline{p}}^c L_{\underline{p}}^c \Pi_{\underline{p}}^c \mathbf{N}_{\underline{p}}^c + \mathcal{R}_{\overline{p}}^c L_{\overline{p}}^c \Pi_{\overline{p}}^c \mathbf{N}_{\overline{p}}^c \right) - \alpha A_c P_c \mathbf{e}_Y \right]. \tag{30}$$

Using this discrete gradient operator, the momentum equation is rewritten

$$m_c \frac{d}{dt} \mathbf{U}_c + \sum_{p \in \mathcal{P}_c} \left(\mathcal{R}_{\underline{p}}^c L_{\underline{p}}^c \Pi_{\underline{p}}^c \mathbf{N}_{\underline{p}}^c + \mathcal{R}_{\overline{p}}^c L_{\overline{p}}^c \Pi_{\overline{p}}^c \mathbf{N}_{\overline{p}}^c \right) - \alpha A_c P_c \mathbf{e}_Y = \mathbf{0}. \tag{31}$$

We have obtained a node-based discretization for the momentum equation which is equivalent to the face flux discretization (14b) provided that the momentum face flux satisfies

$$\mathcal{R}_f^c \Pi_f^c = \frac{1}{2} \left(\frac{2\mathcal{R}_p + \mathcal{R}_p}{3} \Pi_{\overline{p}}^c + \frac{\mathcal{R}_p + 2\mathcal{R}_p}{3} \Pi_{\underline{p}}^c \right).$$

Once again, we note that this condition amounts to a linear interpolation of the pressure along face $f = [p, p]$.

3.5.2. Area-weighted formulation

The discrete gradient operator over the cell Ω_c corresponding to the area-weighted formulation is defined as follows

$$\langle \nabla P \rangle_c^{\mathrm{AW}} = \frac{\overline{\mathcal{R}}_c}{V_c} \sum_{p \in \mathcal{P}_c} \left(L_{\underline{p}}^c \Pi_{\underline{p}}^c \mathbf{N}_{\underline{p}}^c + L_{\overline{p}}^c \Pi_{\overline{p}}^c \mathbf{N}_{\overline{p}}^c \right), \tag{32}$$

where $\overline{\mathcal{R}}_c = \frac{V_c}{A_c}$ is the cell-averaged pseudo radius. We deduce the following discretization for the momentum equation

$$m_c \frac{d}{dt} \mathbf{U}_c + \overline{\mathcal{R}}_c \sum_{p \in \mathcal{P}_c} \left(L_{\underline{p}}^c \Pi_{\underline{p}}^c \mathbf{N}_{\underline{p}}^c + L_{\overline{p}}^c \Pi_{\overline{p}}^c \mathbf{N}_{\overline{p}}^c \right) = \mathbf{0}. \tag{33}$$

This nodal flux discretization of the momentum equation is equivalent to the face flux discretization (19) provided that the momentum face flux satisfies

$$\widehat{\Pi}_f^c = \frac{1}{2} \left(\Pi_{\overline{p}}^c + \Pi_{\underline{p}}^c \right),$$

which corresponds to a linear interpolation of the pressure along the face. Using the definition of the cell-averaged pseudo radius, we note that the momentum equation can be rewritten

$$\mu_c \frac{d}{dt} \mathbf{U}_c + \sum_{p \in \mathcal{P}_c} \left(L_{\underline{p}}^c \Pi_{\underline{p}}^c \mathbf{N}_{\underline{p}}^c + L_{\overline{p}}^c \Pi_{\overline{p}}^c \mathbf{N}_{\overline{p}}^c \right) = \mathbf{0}, \tag{34}$$
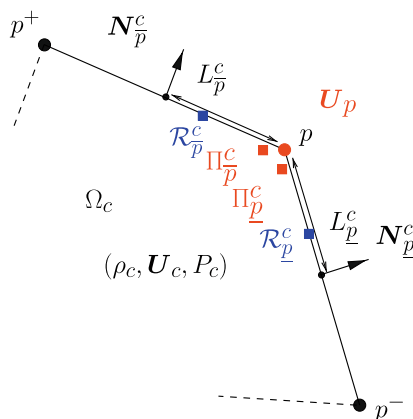

Fig. 5. Localization of the nodal pressures given by the half Riemann problems at point p viewed from cell Ω_c.

recalling that $\mu_c = \rho_c A_c$ is the Cartesian inertia associated with cell Ω_c. We point out that in the case of Cartesian geometry Eqs. (31) and (33) coincide. Hence, both formulations reduce to the classical Cartesian discretization, which has been previously derived in [24,25,23].

3.5.3. Expression of the nodal pressures

To close this section, we show how to express the nodal pressures in terms of the point velocity. Since the velocity of the edges $[p,p^-]$ and $[p,p^+]$, in the vicinity of point p, is equal to the nodal velocity $\boldsymbol{U}_p$, the nodal pressures are computed using the following half approximate Riemann problems

$$P_c - \Pi_{\underline{p}}^c = Z_{\underline{p}}^c (\boldsymbol{U}_p - \boldsymbol{U}_c) \cdot \boldsymbol{N}_{\underline{p}}^c, \tag{35a}$$

$$P_c - \Pi_{\overline{p}}^c = Z_{\overline{p}}^c (\boldsymbol{U}_p - \boldsymbol{U}_c) \cdot \boldsymbol{N}_{\overline{p}}^c. \tag{35b}$$

Here, $Z_{\underline{p}}^c, Z_{\overline{p}}^c$ are mass fluxes swept by the waves. To determine these coefficients we follow the approach suggested by Dukowicz [16] setting

$$Z_{\underline{p}}^c = \rho_c \left[a_c + \Gamma_c |(\boldsymbol{U}_p - \boldsymbol{U}_c) \cdot \boldsymbol{N}_{\underline{p}}^c| \right], \tag{36a}$$

$$Z_{\overline{p}}^c = \rho_c \left[a_c + \Gamma_c |(\boldsymbol{U}_p - \boldsymbol{U}_c) \cdot \boldsymbol{N}_{\overline{p}}^c| \right], \tag{36b}$$

where a_c is the local isentropic speed of sound and Γ_c is a material-dependent parameter that is given in terms of the density ratio in the limit of very strong shocks. In the case of gamma law gas one gets $\Gamma_c = \frac{\gamma+1}{2}$. We note that for $\Gamma_c = 0$, we recover the classical acoustic approximation and the coefficients $Z_{\underline{p}}^c$ and $Z_{\overline{p}}^c$ reduce to the acoustic impedance of the cell Ω_c, which is denoted by Z_c.

Comment 2. Let us consider a uniform fluid flow characterized by the constant state $(\rho_0, \boldsymbol{U}_0, P_0)$. Assuming that the nodal velocity, $\boldsymbol{U}_p$, is equal to the uniform flow velocity, $\boldsymbol{U}_0$, Eq. (35) implies $\Pi_{\underline{p}}^c = \Pi_{\overline{p}}^c = P_0$. Therefore, the discrete gradient operators corresponding to both formulations writes

$$\langle \boldsymbol{\nabla} P_0 \rangle_c^{CV} = \frac{1}{V_c} \left[\sum_{p \in \mathcal{P}(c)} P_0 \left(\mathcal{R}_{\underline{p}}^c L_{\underline{p}}^c \boldsymbol{N}_{\underline{p}}^c + \mathcal{R}_{\overline{p}}^c L_{\overline{p}}^c \boldsymbol{N}_{\overline{p}}^c \right) - \alpha A_c P_0 \boldsymbol{e}_Y \right],$$

$$\langle \boldsymbol{\nabla} P_0 \rangle_c^{AW} = \frac{\overline{\mathcal{R}_c}}{V_c} \sum_{p \in \mathcal{P}(c)} P_0 \left(L_{\underline{p}}^c \boldsymbol{N}_{\underline{p}}^c + L_{\overline{p}}^c \boldsymbol{N}_{\overline{p}}^c \right).$$

Thus, applying the geometric identity (29) for $\alpha = 0$ and $\alpha = 1$, we get $\langle \boldsymbol{\nabla} P_0 \rangle_c^{CV} = \langle \boldsymbol{\nabla} P_0 \rangle_c^{AW} = 0$. This shows that our discrete gradient operators are consistent in the sense that they preserve uniform flows.

3.6. Node-based discretization of the total energy equation

Using the definition of the discrete divergence operator and the nodal pressures previously introduced, we deduce the node-based discretization of the total energy equation

$$m_c \frac{d}{dt} E_c + \sum_{p \in \mathcal{P}(c)} \left(\mathcal{R}_{\underline{p}}^c L_{\underline{p}}^c \Pi_{\underline{p}}^c \boldsymbol{N}_{\underline{p}}^c + \mathcal{R}_{\overline{p}}^c L_{\overline{p}}^c \Pi_{\overline{p}}^c \boldsymbol{N}_{\overline{p}}^c \right) \cdot \boldsymbol{U}_p = 0. \tag{37}$$

We claim that this node-based discretization is equivalent to the face flux discretization (14c) provided that

$$\mathcal{R}_f^c (\Pi \boldsymbol{U})_f^c = \frac{1}{2} \left(\frac{2\mathcal{R}_p + \mathcal{R}_{p^+}}{3} \Pi_{\overline{p}}^c \boldsymbol{U}_p + \frac{\mathcal{R}_p + 2\mathcal{R}_{p^+}}{3} \Pi_{\underline{p}^+}^c \boldsymbol{U}_{p^+} \right).$$

3.7. Construction of a nodal solver

The aim of this section is to construct a nodal solver which shall provide the nodal velocity $\boldsymbol{U}_p$ and the nodal pressures for both formulations. The evaluation of these nodal quantities relies on an argument of total energy conservation.

3.7.1. The issue of total energy conservation

First, let us show why the interface pressure on each face is not uniquely defined on the contrary to the classical finite volume approach. Consider the face $[p,q]$ shared by the cells Ω_c and Ω_d. As it is displayed in Fig. 6, we have introduced two nodal pressures on $[p,q]$ viewed from cell Ω_c: $\Pi_{\overline{p}}^c, \Pi_{\underline{q}}^c$, and two nodal pressures on $[p,q]$ viewed from cell Ω_d: $\Pi_{\underline{p}}^d, \Pi_{\overline{q}}^d$. The nodal pressures related to node p are written according to Eq. (35)

$$P_c - \Pi_{\overline{p}}^c = Z_c (\boldsymbol{U}_p - \boldsymbol{U}_c) \cdot \boldsymbol{N}_{\overline{p}}^c,$$

$$P_d - \Pi_{\underline{p}}^d = Z_d (\boldsymbol{U}_p - \boldsymbol{U}_d) \cdot \boldsymbol{N}_{\underline{p}}^c.$$
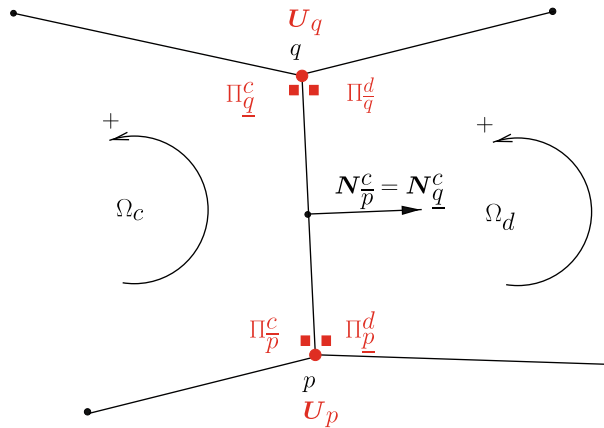
Fig. 6. Nodal pressures related to the face p, q shared by cells Ω_c and Ω_d.

Note that here, in order to simplify the computations, we have used the acoustic approximate Riemann solver, and Z_c, Z_d denote the acoustic impedance of the cells Ω_c and Ω_d. By subtracting the second equation from the first one we obtain

$$\Pi_{\underline{p}}^d \quad \Pi_{\overline{p}}^c \quad Z_c \quad Z_d \left(\boldsymbol{U}_p \cdot \boldsymbol{N}_{\overline{p}}^c \quad \mathcal{V}_{c,d}^\star \right), \tag{38}$$

where $\mathcal{V}_{c,d}^\star$ is the normal component of the Riemann velocity

$$\mathcal{V}_{c,d}^\star \quad \frac{Z_c \boldsymbol{U}_c \quad Z_d \boldsymbol{U}_d}{Z_c \quad Z_d} \cdot \boldsymbol{N}_{\overline{p}}^c \quad \frac{P_d \quad P_c}{Z_c \quad Z_d}.$$

This normal velocity corresponds to the one-dimensional solution of the acoustic Riemann problem in the direction of the unit normal $\boldsymbol{N}_{\overline{p}}^c$. Eq. (38) shows that the nodal pressures are equal if and only if the projection of the node velocity onto the unit normal is equal to the one-dimensional normal component of the Riemann velocity. Since in general $\boldsymbol{U}_p \cdot \boldsymbol{N}_{\overline{p}}^c \neq \mathcal{V}_{c,d}^\star$, we have the discontinuity $\Pi_{\underline{p}}^d \neq \Pi_{\overline{p}}^c$. The discontinuity of these pressures across the face implies the loss of total energy conservation, on the contrary to the 1D Riemann solver classical approach. We shall show hereafter how to recover total energy conservation by imposing an additional constraint which will be the main ingredient to construct the nodal solver.

To address this issue, let us write the global balance of energy without taking into account the boundary conditions. The summation of the total energy Eq. (37) over all the cells leads to

$$\frac{d}{dt} \left(\sum_c m_c \boldsymbol{E}_c \right) \quad \sum_c \sum_{p \in \mathcal{P} c} \left(\mathcal{R}_{\underline{p}}^c L_{\underline{p}}^c \Pi_{\underline{p}}^c \boldsymbol{N}_{\underline{p}}^c \quad \mathcal{R}_{\overline{p}}^c L_{\overline{p}}^c \Pi_{\overline{p}}^c \boldsymbol{N}_{\overline{p}}^c \right) \cdot \boldsymbol{U}_p.$$

Switching the summation over cells and the summation over nodes in the above right-hand side, one gets

$$\frac{d}{dt} \left(\sum_c m_c E_c \right) \quad \sum_p \sum_{c \in \mathcal{C} p} \left(\mathcal{R}_{\underline{p}}^c L_{\underline{p}}^c \Pi_{\underline{p}}^c \boldsymbol{N}_{\underline{p}}^c \quad \mathcal{R}_{\overline{p}}^c L_{\overline{p}}^c \Pi_{\overline{p}}^c \boldsymbol{N}_{\overline{p}}^c \right) \cdot \boldsymbol{U}_p,$$

where $\mathcal{C} p$ is the set of the cells around point p. Total energy is conserved provided that the term between parentheses in the right-hand side is null. This enables us to provide the following sufficient condition which ensures total energy conservation

$$\sum_{c \in \mathcal{C} p} \mathcal{R}_{\underline{p}}^c L_{\underline{p}}^c \Pi_{\underline{p}}^c \boldsymbol{N}_{\underline{p}}^c \quad \mathcal{R}_{\overline{p}}^c L_{\overline{p}}^c \Pi_{\overline{p}}^c \boldsymbol{N}_{\overline{p}}^c \quad \boldsymbol{0}. \tag{39}$$

With this sufficient condition in mind, let us examine the conservation of momentum for the control volume formulation and the area weighted formulation. For the first formulation, the computation of the global balance of momentum, without taking into account the boundary conditions, yields

$$\frac{d}{dt} \left(\sum_c m_c \boldsymbol{U}_c \right) \quad \sum_c \left[\sum_{p \in \mathcal{P} c} \left(\mathcal{R}_{\underline{p}}^c L_{\underline{p}}^c \Pi_{\underline{p}}^c \boldsymbol{N}_{\underline{p}}^c \quad \mathcal{R}_{\overline{p}}^c L_{\overline{p}}^c \Pi_{\overline{p}}^c \boldsymbol{N}_{\overline{p}}^c \right) \quad \alpha A_c P_c \boldsymbol{e}_Y \right].$$

Now, switching the summation over cells and the summation over nodes in right-hand side and using (39) one gets

$$\frac{d}{dt} \left(\sum_c m_c \boldsymbol{U}_c \right) \quad \alpha \left(\sum_c A_c P_c \right) \boldsymbol{e}_Y.$$

This last equation expresses the conservation of momentum for the control volume formulation. Concerning the area-weighted formulation, we point out that it is not possible to exhibit such a global momentum balance. This comes from

the fact that the discrete gradient operator used in the area weighted formulation is not compatible with the sufficient condition (39).

The examination of the left-hand side of Eq. (39) allows a mechanical interpretation by introducing the force

$$\boldsymbol{F}_{pc} = \mathcal{R}_{\underline{p}}^c L_{\underline{p}}^c \Pi_{\underline{p}}^c \boldsymbol{N}_{\underline{p}}^c + \mathcal{R}_{\overline{p}}^c L_{\overline{p}}^c \Pi_{\overline{p}}^c \boldsymbol{N}_{\overline{p}}^c. \tag{40}$$

This force is a sub-cell force which acts at point p and is related to cell Ω_c. Thus, the sufficient condition (39) can be viewed as mechanical balance of the sub-cell forces around point p. Now, substituting the expressions of the nodal pressures given by the half Riemann problems (35), the sub-cell force is rewritten

$$\boldsymbol{F}_{pc} = \left(\mathcal{R}_{\underline{p}}^c L_{\underline{p}}^c \boldsymbol{N}_{\underline{p}}^c + \mathcal{R}_{\overline{p}}^c L_{\overline{p}}^c \boldsymbol{N}_{\overline{p}}^c \right) P_c + \mathsf{M}_{pc} (\boldsymbol{U}_p - \boldsymbol{U}_c), \tag{41}$$

where M_{pc} is the 2×2 matrix defined by

$$\mathsf{M}_{pc} = Z_{\underline{p}}^c \mathcal{R}_{\underline{p}}^c L_{\underline{p}}^c \, \boldsymbol{N}_{\underline{p}}^c \otimes \boldsymbol{N}_{\underline{p}}^c + Z_{\overline{p}}^c L_{\overline{p}}^c \mathcal{R}_{\overline{p}}^c \, \boldsymbol{N}_{\overline{p}}^c \otimes \boldsymbol{N}_{\overline{p}}^c . \tag{42}$$

We remark that this matrix is symmetric positive definite, thus always invertible. Finally, using these notations, the sufficient condition (39) can be rewritten under the equivalent form

$$\sum_{c \in \mathcal{C}(p)} \left(\mathcal{R}_{\underline{p}}^c L_{\underline{p}}^c \boldsymbol{N}_{\underline{p}}^c + \mathcal{R}_{\overline{p}}^c L_{\overline{p}}^c \boldsymbol{N}_{\overline{p}}^c \right) P_c + \mathsf{M}_{pc} (\boldsymbol{U}_p - \boldsymbol{U}_c) = \boldsymbol{0}. \tag{43}$$

The sufficient condition to ensure total energy conservation exhibits, in its final form, a vectorial equation satisfied by the point velocity $\boldsymbol{U}_p$. This equation allows to construct a nodal solver.

3.7.2. Computation of the nodal velocity

There remains to compute the nodal velocity using Eq. (43). Setting $\mathsf{M}_p = \sum_{c \in \mathcal{C}(p)} \mathsf{M}_{pc}$ the system satisfied by the point velocity $\boldsymbol{U}_p$ is written

$$\mathsf{M}_p \boldsymbol{U}_p = \sum_{c \in \mathcal{C}(p)} \left(\mathcal{R}_{\underline{p}}^c L_{\underline{p}}^c \boldsymbol{N}_{\underline{p}}^c + \mathcal{R}_{\overline{p}}^c L_{\overline{p}}^c \boldsymbol{N}_{\overline{p}}^c \right) P_c + \mathsf{M}_{pc} \boldsymbol{U}_c. \tag{44}$$

We remark that the M_p matrix is symmetric positive definite by construction, hence it is always invertible. If we use the acoustic approximation (coefficient $\Gamma_c = 0$ in Eq. (36)), the mass swept fluxes reduce to the acoustic impedance, i.e. $Z_{\underline{p}}^c = Z_{\overline{p}}^c = Z_c$, then the system (44) becomes linear and it admits a unique solution. In the general case corresponding to $\Gamma_c \neq 0$, system (44) is non-linear due to the dependence of the mass swept fluxes to the point velocity. Therefore, $\boldsymbol{U}_p$ has to be computed by using an iterative procedure such as a fixed point algorithm. From a theoretical point of view, we cannot show the convergence of such an algorithm. However, in numerical applications, we have found that few iterations are needed to get the convergence. Regardless of the type of approximation used, the expressions for the point velocity and the nodal pressure can be written

$$\boldsymbol{U}_p = \mathsf{M}_p^{-1} \sum_{c \in \mathcal{C}(p)} \left(\mathcal{R}_{\underline{p}}^c L_{\underline{p}}^c \boldsymbol{N}_{\underline{p}}^c + \mathcal{R}_{\overline{p}}^c L_{\overline{p}}^c \boldsymbol{N}_{\overline{p}}^c \right) P_c + \mathsf{M}_{pc} \boldsymbol{U}_c, \tag{45a}$$

$$P_c = \Pi_{\underline{p}}^c + Z_{\underline{p}}^c (\boldsymbol{U}_p - \boldsymbol{U}_c) \cdot \boldsymbol{N}_{\underline{p}}^c, \tag{45b}$$

$$P_c = \Pi_{\overline{p}}^c + Z_{\overline{p}}^c (\boldsymbol{U}_p - \boldsymbol{U}_c) \cdot \boldsymbol{N}_{\overline{p}}^c. \tag{45c}$$

Finally, using total energy conservation and half Riemann problems, we have constructed a two-dimensional nodal solver, which can be viewed as a two-dimensional extension of the classical one-dimensional Riemann solver. This nodal solver is suitable for both control volume and area-weighted formulations. We notice that in the case of Cartesian geometry, it reduces to the nodal solver which has been derived in [24,23].

Comment 3. We emphasize that the main difference between the present nodal solver and the previous one derived in [24,23] lies in the presence of the $\mathcal{R}_{\underline{p}}^c, \mathcal{R}_{\overline{p}}^c$ factors in the nodal velocity expression, refer to (45a). These geometric factors come from the compatible definition of the discrete gradient operator (adjointness with the discrete divergence operator).

3.7.3. The case of a one-dimensional spherical flow in cylindrical geometry

Here, we show that our nodal solver preserves the spherical symmetry in the case of a one-dimensional spherical flow computed on an equal angle polar grid such as the one displayed in Fig. 7. Let us consider the point p surrounded by the four quadrangular cells $\Omega_i, i = 1, \ldots, 4$. To simplify the computation, we use the orthonormal basis $(\boldsymbol{e}_r, \boldsymbol{e}_\theta)$ located at point p. Due to the symmetry of the flow, the thermodynamical quantities are equal in the cells Ω_1, Ω_4 and in the cells Ω_2, Ω_3. The cell-centered velocities write $\boldsymbol{U}_1 = U_1 \boldsymbol{N}_{1,2}, \boldsymbol{U}_4 = U_1 \boldsymbol{N}_{3,4}, \boldsymbol{U}_2 = U_2 \boldsymbol{N}_{1,2}, \boldsymbol{U}_3 = U_2 \boldsymbol{N}_{3,4}$. Here, $\boldsymbol{N}_{i,i+1}$ denotes the counterclockwise oriented unit normal of the interface shared by cells Ω_i, Ω_{i+1} and U_i is the velocity magnitude in cell Ω_i. In the local basis $(\boldsymbol{e}_r, \boldsymbol{e}_\theta)$ we have

$$\boldsymbol{N}_{1,2} \begin{pmatrix} \cos\frac{\Delta\theta}{2} \\ \sin\frac{\Delta\theta}{2}, \end{pmatrix}, \quad \boldsymbol{N}_{2,3} \begin{pmatrix} 0 \\ 1 \end{pmatrix}, \quad \boldsymbol{N}_{3,4} \begin{pmatrix} \cos\frac{\Delta\theta}{2} \\ \sin\frac{\Delta\theta}{2} \end{pmatrix}, \quad \boldsymbol{N}_{4,1} \begin{pmatrix} 0 \\ 1 \end{pmatrix}.$$

Now, using the acoustic approximation, we evaluate the M_p matrix and $\boldsymbol{R}H$ vector which corresponds to the right-hand side of (45a). The point velocity is the solution of the linear system $M_p\boldsymbol{U}_p$ $\boldsymbol{R}H$. Some elementary calculations provide the elements of the matrix M_p

$$M_{p,rr} \quad Z_1 \quad Z_2 \, L_{1,2} \, \mathcal{R}_{1,2} \quad \mathcal{R}_{3,4} \, \cos^2\frac{\Delta\theta}{2},$$

$$M_{p,r\theta} \quad M_{p,\theta r} \quad Z_1 \quad Z_2 \, L_{1,2} \, \mathcal{R}_{3,4} \quad \mathcal{R}_{1,2} \, \cos\frac{\Delta\theta}{2}\sin\frac{\Delta\theta}{2},$$

$$M_{p,\theta\theta} \quad Z_1 \quad Z_2 \, L_{1,2} \, \mathcal{R}_{1,2} \quad \mathcal{R}_{3,4} \, \sin^2\frac{\Delta\theta}{2} \quad 2\, Z_1 L_{4,1} \mathcal{R}_{4,1} \quad Z_2 L_{2,3} \mathcal{R}_{2,3} \,.$$

The components of the right-hand side write

$$RH_r \quad Z_1 U_1 \quad Z_2 U_2 \quad P_2 \quad P_1 \, L_{1,2} \, \mathcal{R}_{1,2} \quad \mathcal{R}_{3,4} \, \cos\frac{\Delta\theta}{2},$$

$$RH_\theta \quad Z_1 U_1 \quad Z_2 U_2 \quad P_2 \quad P_1 \, L_{1,2} \, \mathcal{R}_{3,4} \quad \mathcal{R}_{1,2} \, \sin\frac{\Delta\theta}{2}.$$

Here, $L_{i,i\ 1}$ and $\mathcal{R}_{i,i\ 1}$ denote the half length and the pseudo radius related to the edge shared by the cells Ω_i and $\Omega_{i\ 1}$. We notice that $L_{1,2}$ $L_{3,4}$ due to the symmetry of the grid. Finally, we get the following result for the components of the point velocity expressed in the local basis $\boldsymbol{e}_r, \boldsymbol{e}_\theta$

$$u_{p,r} \quad \frac{Z_1 U_1 \quad Z_2 U_2 \quad P_2 \quad P_1}{Z_1 \quad Z_2} \frac{1}{\cos\frac{\Delta\theta}{2}}, \quad u_{p,\theta} \quad 0.$$

The point velocity is radial, hence the nodal solver preserves the spherical symmetry on equal angle polar grid. We have recovered the classical one-dimensional acoustic Godunov solver modified by a geometrical factor which corresponds to the projection of the cell velocity direction onto the radial vector $\boldsymbol{e}_r$. This geometrical factor has no consequence since $\cos\frac{\Delta\theta}{2} \to 1$ when $\Delta\theta \to 0$. We point out that the symmetry preservation is due to the fact that the mesh is equally spaced in the angular direction. If the mesh does not satisfy this assumption, then $L_{1,2} \neq L_{3,4}$ and $u_{p,\theta} \neq 0$.

To achieve this study, we provide the computation of the eight nodal pressures located at point p, refer to Fig. 8. There are two nodal pressures for each cell surrounding point p, each pressure being associated with the unit outward normal. Hence, with the present notations, for the cell Ω_i these pressures are determined as follows
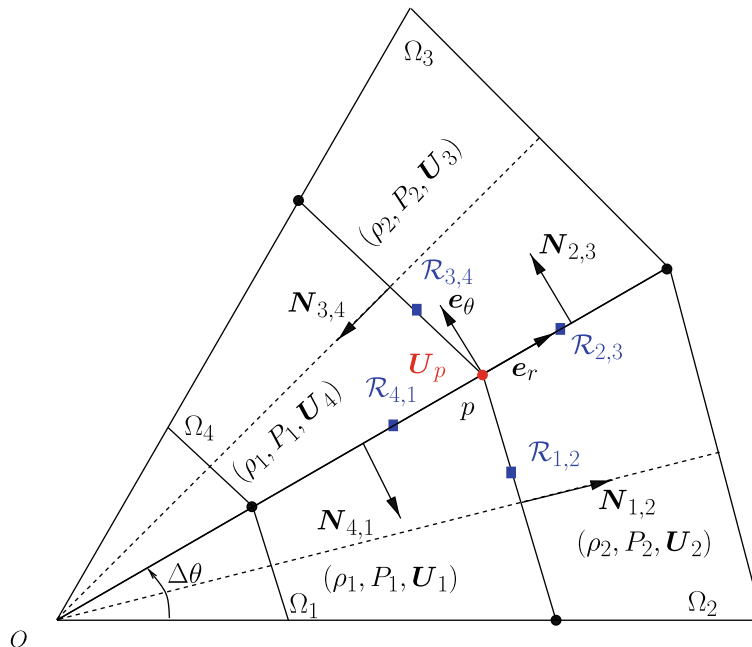

Fig. 7. Fragment of an equal angle polar grid and notations for a one-dimensional spherical flow.

$$\Pi_{\underline{p}}^i = P_i - Z_i \left(\boldsymbol{U}_p - \boldsymbol{U}_i \right) \cdot \boldsymbol{N}_{i,i+1},$$

$$\Pi_{\bar{p}}^i = P_i - Z_i \left(\boldsymbol{U}_p - \boldsymbol{U}_i \right) \cdot \boldsymbol{N}_{i-1,i}.$$

Using the expression of the point velocity $\boldsymbol{U}_p$, some elementary algebra leads to

$$\Pi_{\underline{p}}^1 = \Pi_{\bar{p}}^2 = \frac{Z_2 P_1 + Z_1 P_2 - Z_1 Z_2 \left(U_2 - U_1 \right)}{Z_1 + Z_2},$$

$$\Pi_{\underline{p}}^2 = \Pi_{\bar{p}}^3 = P_2 - Z_2 U_2 \sin\frac{\Delta\theta}{2},$$

$$\Pi_{\underline{p}}^3 = \Pi_{\bar{p}}^4 = \frac{Z_2 P_1 + Z_1 P_2 - Z_1 Z_2 \left(U_2 - U_1 \right)}{Z_1 + Z_2},$$

$$\Pi_{\underline{p}}^4 = \Pi_{\bar{p}}^1 = P_1 + Z_1 U_1 \sin\frac{\Delta\theta}{2}.$$

We note that the nodal pressures located on the two sides of the same edge are equal. For the two edges corresponding to $\Omega_1 \cap \Omega_2$ and $\Omega_3 \cap \Omega_4$, we remark that the nodal pressures are exactly equal to the interface pressure computed from an acoustic Riemann solver. The remaining edges, which are perpendicular to the angular direction, separate two identical states, hence the corresponding nodal pressures should coincide with them. However, we notice that the nodal pressure differs from the constant state up to a geometric factor which is proportional to $\sin\frac{\Delta\theta}{2}$. We observe that this geometric factor will introduce a viscous term which acts in the angular direction. This term has two bad consequences. Firstly, it implies the loss of symmetry for the control volume scheme as it has been explained in Section 3.3. Secondly, it prevents our first order scheme from ensuring the wave front invariance requirement [10]. This shortcoming can be overcome using a high-order extension, in which the nodal solver uses the extrapolated pressure and velocities at the point, rather than their averaged-cell values.

3.8. Summary of the node-based flux discretization

We summarize the previous results recalling, for both control volume and area weighted formulations, the semi-discrete evolution equations that constitute a closed set for the unknowns $\left(\frac{1}{\rho_c}, \boldsymbol{U}_c, E_c \right)$. First, we write the system which corresponds to the control volume formulation

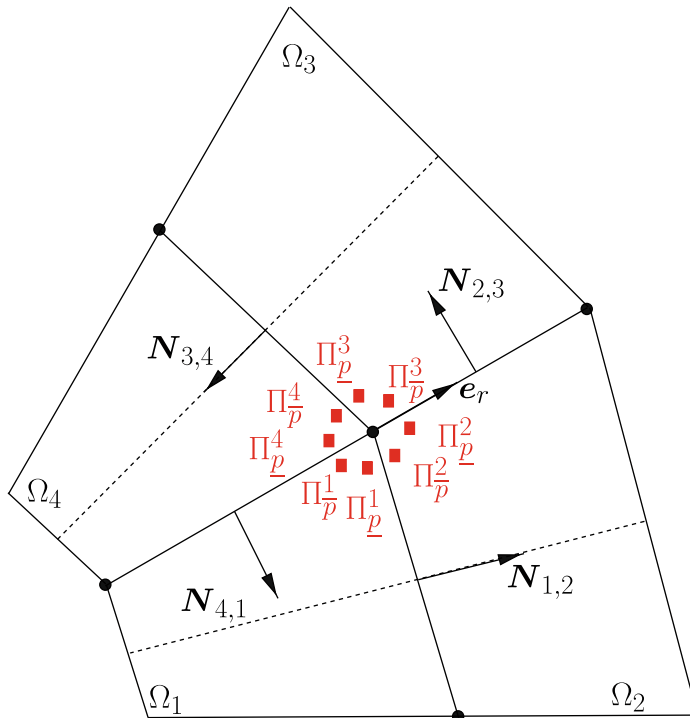**Fig. 8.** Localization of the multiple nodal pressures around point *p*.

$$m_c \frac{d}{dt}\left(\frac{1}{\rho_c}\right) - \sum_{p \in \mathcal{P}_c} \left(\mathcal{R}_{\underline{p}}^c L_{\underline{p}}^c \boldsymbol{N}_{\underline{p}}^c + \mathcal{R}_{\overline{p}}^c L_{\overline{p}}^c \boldsymbol{N}_{\overline{p}}^c\right) \cdot \boldsymbol{U}_p = 0,$$

$$m_c \frac{d}{dt}\boldsymbol{U}_c + \sum_{p \in \mathcal{P}_c} \left(\mathcal{R}_{\underline{p}}^c L_{\underline{p}}^c \Pi_{\underline{p}}^c \boldsymbol{N}_{\underline{p}}^c + \mathcal{R}_{\overline{p}}^c L_{\overline{p}}^c \Pi_{\overline{p}}^c \boldsymbol{N}_{\overline{p}}^c\right) - \alpha A_c P_c \boldsymbol{e}_Y = \boldsymbol{0},$$

$$m_c \frac{d}{dt}E_c + \sum_{p \in \mathcal{P}_c} \left(\mathcal{R}_{\underline{p}}^c L_{\underline{p}}^c \Pi_{\underline{p}}^c \boldsymbol{N}_{\underline{p}}^c + \mathcal{R}_{\overline{p}}^c L_{\overline{p}}^c \Pi_{\overline{p}}^c \boldsymbol{N}_{\overline{p}}^c\right) \cdot \boldsymbol{U}_p = 0.$$

To obtain the area weighted formulation, it is sufficient to replace the above discrete momentum equation by the following one

$$m_c \frac{d}{dt}\boldsymbol{U}_c + \overline{\mathcal{R}}_c \sum_{p \in \mathcal{P}_c} L_{\underline{p}}^c \Pi_{\underline{p}}^c \boldsymbol{N}_{\underline{p}}^c + L_{\overline{p}}^c \Pi_{\overline{p}}^c \boldsymbol{N}_{\overline{p}}^c = \boldsymbol{0}.$$

We notice that the discrete kinematic equation and the nodal solver are common to both formulations. The local kinematic equation is written

$$\frac{d}{dt}\boldsymbol{X}_p = \boldsymbol{U}_p, \quad \boldsymbol{X}_p(0) = \boldsymbol{x}_p,$$

The point velocity $\boldsymbol{U}_p$ and the nodal pressures are obtained thanks to the nodal solver defined by

$$\boldsymbol{U}_p = \mathsf{M}_p^{-1} \sum_{c \in \mathcal{C}_p} \left[\left(\mathcal{R}_{\underline{p}}^c L_{\underline{p}}^c \boldsymbol{N}_{\underline{p}}^c + \mathcal{R}_{\overline{p}}^c L_{\overline{p}}^c \boldsymbol{N}_{\overline{p}}^c\right)P_c + \mathsf{M}_{pc}\boldsymbol{U}_c\right],$$

$$P_c = \Pi_{\underline{p}}^c + Z_{\underline{p}}^c (\boldsymbol{U}_p - \boldsymbol{U}_c) \cdot \boldsymbol{N}_{\underline{p}}^c,$$

$$P_c = \Pi_{\overline{p}}^c + Z_{\overline{p}}^c (\boldsymbol{U}_p - \boldsymbol{U}_c) \cdot \boldsymbol{N}_{\overline{p}}^c,$$

where the 2×2 matrices, M_{pc} and M_p, are written

$$\mathsf{M}_{pc} = Z_{\underline{p}}^c \mathcal{R}_{\underline{p}}^c L_{\underline{p}}^c \ \boldsymbol{N}_{\underline{p}}^c \otimes \boldsymbol{N}_{\underline{p}}^c + Z_{\overline{p}}^c \mathcal{R}_{\overline{p}}^c L_{\overline{p}}^c \left(\boldsymbol{N}_{\overline{p}}^c \otimes \boldsymbol{N}_{\overline{p}}^c\right), \quad \mathsf{M}_p = \sum_{c \in \mathcal{C}_p} \mathsf{M}_{pc}.$$

We recall that the swept mass fluxes $Z_{\underline{p}}^c$ and $Z_{\overline{p}}^c$ are defined by (36).

Finally, we have obtained a first-order cell-centered discretization of the Lagrangian hydrodynamics equations using a node-based flux discretization. *The fluxes and the mesh motion are computed in a compatible way thanks to a nodal solver that uniquely provides the point velocity and the nodal pressures.* The area-weighted scheme preserves the spherical symmetry on an equal angle polar grid whereas the control volume scheme does not. We also notice that both formulations reduce to the scheme which has been derived in [23], in the case of the Cartesian geometry.

Comment 4. In the Lagrangian formalism, we have to consider two types of boundary conditions on the border of the domain $\mathcal{D}$: either the pressure or the normal component of the velocity is prescribed. Here, we do not detail the implementation of these boundary conditions. Let us notice that they are consistent with our nodal solver. For a detailed presentation about this topic the reader can refer to [24].

3.9. Entropy inequality for the control volume formulation

We show that our first-order control volume scheme in its semi-discrete form satisfies a local entropy inequality. Using the Gibbs formula [14], we compute the time rate of change of the specific entropy σ_c in cell Ω_c

$$m_c T_c \frac{d\sigma_c}{dt} = m_c\left[\frac{d\varepsilon_c}{dt} + P_c \frac{d}{dt}\left(\frac{1}{\rho_c}\right)\right], \tag{46}$$

where T_c denotes the mean temperature of the cell. Thanks to the definition of the internal energy this equation is rewritten

$$m_c T_c \frac{d\sigma_c}{dt} = m_c\left[\frac{dE_c}{dt} - \boldsymbol{U}_c \cdot \frac{d\boldsymbol{U}_c}{dt} + P_c \frac{d}{dt}\left(\frac{1}{\rho_c}\right)\right].$$

We dot-multiply momentum Eq. (31) by $\boldsymbol{U}_c$ and subtract it from the total energy Eq. (37) to get

$$m_c\left[\frac{dE_c}{dt} - \boldsymbol{U}_c \cdot \frac{d\boldsymbol{U}_c}{dt}\right] = -\sum_{p \in \mathcal{P}_c} \left(\mathcal{R}_{\underline{p}}^c L_{\underline{p}}^c \Pi_{\underline{p}}^c \boldsymbol{N}_{\underline{p}}^c + \mathcal{R}_{\overline{p}}^c L_{\overline{p}}^c \Pi_{\overline{p}}^c \boldsymbol{N}_{\overline{p}}^c\right) \cdot (\boldsymbol{U}_p - \boldsymbol{U}_c) - \alpha A_c P_c \boldsymbol{U}_c \cdot \boldsymbol{e}_Y.$$

The pressure work is computed by multiplying (27) by P_c

$$P_c m_c \frac{d}{dt}\left(\frac{1}{\rho_c}\right) = \sum_{p \in \mathcal{P}_c} \left(\mathcal{R}_{\underline{p}}^c L_{\underline{p}}^c P_c \boldsymbol{N}_{\underline{p}}^c + \mathcal{R}_{\overline{p}}^c L_{\overline{p}}^c P_c \boldsymbol{N}_{\overline{p}}^c\right) \cdot \boldsymbol{U}_p = \sum_{p \in \mathcal{P}_c} \left(\mathcal{R}_{\underline{p}}^c L_{\underline{p}}^c P_c \boldsymbol{N}_{\underline{p}}^c + \mathcal{R}_{\overline{p}}^c L_{\overline{p}}^c P_c \boldsymbol{N}_{\overline{p}}^c\right) \cdot (\boldsymbol{U}_p - \boldsymbol{U}_c) + \alpha A_c P_c \boldsymbol{U}_c \cdot \boldsymbol{e}_Y.$$

The last line of the previous equation comes from the geometric identity

$$\sum_{p\in\mathcal{P}_c} \left(\mathcal{R}^c_{\underline{p}}L^c_{\underline{p}}\boldsymbol{N}^c_{\underline{p}} \quad \mathcal{R}^c_{\bar{p}}L^c_{\bar{p}}\boldsymbol{N}^c_{\bar{p}}\right) \quad \alpha A_c\boldsymbol{e}_Y.$$

Finally, the combination of the previous results leads to

$$m_cT_c\frac{d\sigma_c}{dt} \quad \sum_{p\in\mathcal{P}_c} \left[\mathcal{R}^c_{\underline{p}}L^c_{\underline{p}}\left(P_c \quad \Pi^c_{\underline{p}}\right)\boldsymbol{N}^c_{\underline{p}} \quad \mathcal{R}^c_{\bar{p}}L^c_{\bar{p}}\left(P_c \quad \Pi^c_{\bar{p}}\right)\boldsymbol{N}^c_{\bar{p}}\right] \cdot \boldsymbol{U}_p \quad \boldsymbol{U}_c . \tag{47}$$

With the help of the half Riemann problems (35), we deduce the final expression for the time rate of change of the specific entropy within cell Ω_c

$$m_cT_c\frac{d\sigma_c}{dt} \quad \sum_{p\in\mathcal{P}_c} \mathsf{M}_{pc} \boldsymbol{U}_p \quad \boldsymbol{U}_c \cdot \boldsymbol{U}_p \quad \boldsymbol{U}_c . \tag{48}$$

Since the 2×2 matrix M_{pc} is symmetric positive definite, the right-hand side of (48) is a quadratic form which is always positive. Consequently, our control volume scheme is such that entropy increases in the cell Ω_c, that is $\frac{d\sigma_c}{dt} \geqslant 0$. This important property ensures that the kinetic energy is properly dissipated into internal energy. The examination of (48) right-hand side shows a tensorial structure of the entropy dissipation rate which is quite similar to the artificial viscosity used in two-dimensional staggered Lagrangian schemes [8,10].

3.10. Entropy inequality for the area weighted formulation

We note that it is not possible to write such an entropy inequality for the area-weighted scheme. This impossibility comes from the fact that the discrete gradient operator associated with this scheme is not compatible with the discrete divergence operator.

Comment 5. We must admit that our entropy production term is always active even in the case of isentropic flows. For such flows our scheme does not conserve entropy. This property is typical from Godunov-type schemes. However, this extra entropy production can be dramatically decreased by using a high-order extension of the scheme as we shall see in Section 6.

4. The two-dimensional high-order extension

We present a two-dimensional high-order extension for both control volume and area-weighted schemes. This high-order extension uses a one-step time integrator based on the so-called GRP (Generalized Riemann Problem) methodology which has been derived by Ben-Artzi and Falcovitz [4–6]. This methodology consists in solving the higher-order Riemann problem with piecewise linear polynomials, whereby the approximate solution is given as a time power series expansion right at the interface, thus providing a numerical flux for a high-order Godunov-type method. Ben-Artzi and Falcovitz have developed GRP schemes for the one-dimensional compressible gas dynamics equations written in Lagrangian and Eulerian formalisms. In [6], they have also presented a two-dimensional extension using the Strang directional splitting. In the present study, we develop an original genuinely two-dimensional Lagrangian extension which uses the node-based flux discretization previously described. Our derivation employs the acoustic approximation of the GRP method. This approximation provides a framework in which the solution of the GRP is simple to compute and easy to handle. In the Lagrangian one-dimensional case, this approximation has been thoroughly described in the monograph [6], we have also recalled it in [23]. We note that a Riemann invariants approach could have been also used, following the methodology developed in [21].

In what follows, we describe the main algorithm for the two-dimensional Lagrangian hydrodynamics, which allows a straightforward implementation of our high-order extension. Then, we detail the crucial step corresponding to the computation of the time derivatives of the node-based fluxes.

4.1. Description of the GRP algorithm

Let $\left(\frac{1}{\rho^n_c},\boldsymbol{U}^n_c,E^n_c\right)$ be the mass-averaged values of $\left(\frac{1}{\rho},\boldsymbol{U},E\right)$ over the cell Ω^n_c at time t t^n. We assume that all the geometric quantities are known at time t^n. We describe the two-dimensional implementation of the GRP scheme through the following four steps.

Step 0. Construct a piecewise monotone linear representation of the velocity field and the pressure over the cell Ω^n_c at time t^n

$$\boldsymbol{U}_c \boldsymbol{X} \quad \boldsymbol{U}^n_c \quad \boldsymbol{U}_c \cdot (\boldsymbol{X} \quad \boldsymbol{X}^n_c),$$
$$P_c \boldsymbol{X} \quad P^n_c \quad \nabla P_c \cdot (\boldsymbol{X} \quad \boldsymbol{X}^n_c),$$

where $\boldsymbol{X}^n_c$ denotes the centroid of Ω^n_c, $\boldsymbol{U}_c$ and ∇P_c are respectively the piecewise constant velocity and pressure gradients in Ω^n_c.

Step 1. Being given the piecewise linear pressure and velocity at time t^n over the cell Ω_c^n, we solve the Riemann problem for the two-dimensional gas dynamic equations at each point p. With the help of the nodal solver previously developed, determine the point velocity $\boldsymbol{U}_p^n$ and the nodal pressures $\Pi_{\underline{p}}^{c,n}$, $\Pi_{\overline{p}}^{c,n}$ using the extrapolated pressure and velocity at point p

$$\boldsymbol{U}_p^n = \left(\mathsf{M}_p^n\right)^{-1} \sum_{c \in \mathcal{C}_p} \left[\left(\mathcal{R}_{\underline{p}}^{c,n} L_{\underline{p}}^{c,n} \boldsymbol{N}_{\underline{p}}^{c,n} + \mathcal{R}_{\overline{p}}^{c,n} L_{\overline{p}}^{c,n} \boldsymbol{N}_{\overline{p}}^{c,n}\right) P_c\left(\boldsymbol{X}_p^n\right) + \mathsf{M}_{pc}^n \boldsymbol{U}_c\left(\boldsymbol{X}_p^n\right)\right],$$

$$P_c\left(\boldsymbol{X}_p^n\right) - \Pi_{\underline{p}}^{c,n} = Z_{\underline{p}}^{c,n}\left[\boldsymbol{U}_p^n - \boldsymbol{U}_c\left(\boldsymbol{X}_p^n\right)\right] \cdot \boldsymbol{N}_{\underline{p}}^{c,n},$$

$$P_c\left(\boldsymbol{X}_p^n\right) - \Pi_{\overline{p}}^{c,n} = Z_{\overline{p}}^{c,n}\left[\boldsymbol{U}_p^n - \boldsymbol{U}_c\, \boldsymbol{X}_p^n\right] \cdot \boldsymbol{N}_{\overline{p}}^{c,n}.$$

Here, the superscript n is used for geometrical quantities such as lengths and normals to emphasize the fact that they are evaluated at time t^n.

Step 2. Determine the time derivatives $\left(\frac{d\boldsymbol{U}}{dt}\right)_p^n, \left(\frac{d\Pi}{dt}\right)_{\underline{p}}^{c,n}, \left(\frac{d\Pi}{dt}\right)_{\overline{p}}^{c,n}, \left(\frac{dP}{dt}\right)_c^n$ and compute the midpoint values

$$\boldsymbol{U}_p^{n+\frac{1}{2}} = \boldsymbol{U}_p^n + \frac{\Delta t}{2}\left(\frac{d\boldsymbol{U}}{dt}\right)_p^n, \tag{49a}$$

$$\Pi_{\underline{p}}^{c,n+\frac{1}{2}} = \Pi_{\underline{p}}^{c,n} + \frac{\Delta t}{2}\left(\frac{d\Pi}{dt}\right)_{\underline{p}}^{c,n}, \tag{49b}$$

$$\Pi_{\overline{p}}^{c,n+\frac{1}{2}} = \Pi_{\overline{p}}^{c,n} + \frac{\Delta t}{2}\left(\frac{d\Pi}{dt}\right)_{\overline{p}}^{c,n}, \tag{49c}$$

$$P_c^{n+\frac{1}{2}} = P_c^n + \frac{\Delta t}{2}\left(\frac{dP}{dt}\right)_c^n. \tag{49d}$$

Here, we have introduced the time derivatives corresponding to the node-based fluxes $\boldsymbol{U}_p, \Pi_{\underline{p}}^c$ and $\Pi_{\overline{p}}^c$ defined at point p. We have also introduced the time derivative of the cell pressure, P_c, that will be used in the momentum equation for the control volume scheme.

Step 3. Compute the motion of the mesh thanks to the discrete kinematic equation

$$\boldsymbol{X}_p^{n+1} = \boldsymbol{X}_p^n + \Delta t \boldsymbol{U}_p^{n+\frac{1}{2}}, \tag{50}$$

and update the geometrical quantities. Then, evaluate the new averaged values $\left(\frac{1}{\rho_c^{n+1}}, \boldsymbol{U}_c^{n+1}, E_c^{n+1}\right)$ using the updating formulae

$$\rho_c^{n+1} = \frac{m_c}{V_c^{n+1}},$$

$$m_c \boldsymbol{U}_c^{n+1} = \boldsymbol{U}_c^n + \Delta t \sum_{p \in \mathcal{P}_c} \left[\mathcal{R}_{\underline{p}}^{c,n} L_{\underline{p}}^{c,n} \Pi_{\underline{p}}^{c,n+\frac{1}{2}} \boldsymbol{N}_{\underline{p}}^{c,n} + \mathcal{R}_{\overline{p}}^{c,n} L_{\overline{p}}^{c,n} \Pi_{\overline{p}}^{c,n+\frac{1}{2}} \boldsymbol{N}_{\overline{p}}^{c,n}\right]_{c+1}$$

The density computed from this equation is rigorously the same than that computed from mass conservation provided that the time integral of the node area vector is computed exactly. This requirement is fulfilled if one employs the Simpson's rule to define the numerical integration, i.e.

$$\sum_{p\in\mathcal{P}_c}\int_{t^n}^{t^{n+1}}\mathscr{A}_p^c(t)\,dt=\frac{\Delta t}{6}\left[\mathscr{A}_p^c(t^n)+4\mathscr{A}_p^c\left(t^{n+\frac{1}{2}}\right)+\mathscr{A}_p^c(t^{n+1})\right],$$

where $t^{n+\frac{1}{2}}=t^n+\frac{\Delta t}{2}$, since this quadrature rule is exact for quadratic functions. For the momentum and the total energy equations, we have used the geometrical quantities evaluated at the beginning of the time step in order to rigorously ensure the conservativity of the scheme. This last point shall be explained in the subsequent section.

In what follows, we are going to detail step 2, knowing that the monotone piecewise linear reconstruction has already been described in [23]. Let us recall that this piecewise linear reconstruction is performed using a least squares method, followed by a multi-dimensional slope limitation procedure, which is known as the Barth–Jespersen limitation [2,3].

4.2. Computation of the time derivatives

For sake of completeness, we recall the explanations that have been firstly introduced in [23].

4.2.1. Characteristic equations
The first step for computing the time derivatives, consists in writing the characteristic equations for the two-dimensional gas dynamics equations [18]. We recall that by using the nonconservative variables $P,\boldsymbol{U},\sigma$, the gas dynamics equation can be written in nonconservative form

$$\frac{dP}{dt}+\rho a^2\nabla\cdot\boldsymbol{U}=0,\tag{51a}$$

$$\frac{d\boldsymbol{U}}{dt}+\frac{1}{\rho}\nabla P=\boldsymbol{0},\tag{51b}$$

$$\frac{d\sigma}{dt}=0,\tag{51c}$$

where σ denotes the specific entropy. Let $\boldsymbol{N}=(N_X,N_Y)^t$ denote a particular vector of $\mathbb{R}^2$. The Jacobian matrix in the direction $\boldsymbol{N}$ related to the previous system is written

$$A(\boldsymbol{N})=\begin{pmatrix}0 & \rho a^2 N_X & \rho a^2 N_Y & 0\\ \frac{N_X}{\rho} & 0 & 0 & 0\\ \frac{N_Y}{\rho} & 0 & 0 & 0\\ 0 & 0 & 0 & 0\end{pmatrix}.$$

The eigenvalues are easily found to be 0 and $\pm a|\boldsymbol{N}|$. Thus, we have two simple eigenvalues, which for $|\boldsymbol{N}|=1$ are $\lambda=\pm a$ associated with acoustic waves, and $\lambda=0$ of multiplicity 2 associated with the entropy waves. To obtain the characteristic equations in the direction $\boldsymbol{N}$ associated with the acoustic waves, we dot-multiply Eq. (51b) by $\pm\rho a\boldsymbol{N}$ and add it to Eq. (51a) to get
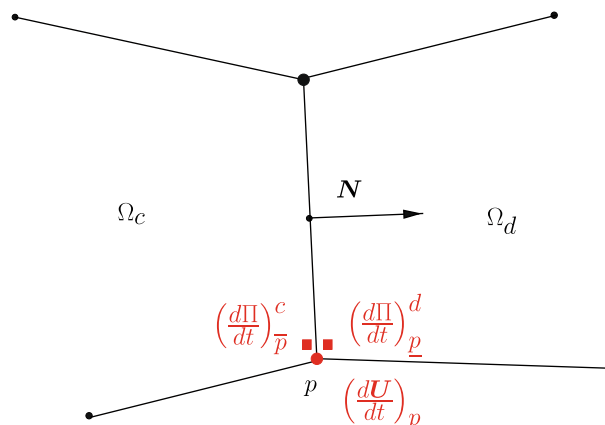

Fig. 9. Generalized Riemann problem at point p.

$$\frac{dP}{dt} \quad a\nabla P \cdot \boldsymbol{N} \quad \rho a\left(\frac{d\boldsymbol{U}}{dt} \cdot \boldsymbol{N} \quad a \quad \cdot \boldsymbol{U}\right) \quad 0, \quad \text{associated with eigenvalue } a, \tag{52a}$$

$$\frac{dP}{dt} \quad a\nabla P \cdot \boldsymbol{N} \quad \rho a\left(\frac{d\boldsymbol{U}}{dt} \cdot \boldsymbol{N} \quad a \quad \cdot \boldsymbol{U}\right) \quad 0, \quad \text{associated with eigenvalue} \quad a, \tag{52b}$$

where $\boldsymbol{N}$ denotes any unit vector.

4.2.2. Construction of a nodal acoustic GRP solver

The second step consists in solving the acoustic GRP problem in the framework of our nodal solver. At time $t \quad t^n$, let us consider a point p and assume that the flow variables in the surrounding cells are all continuous at $\boldsymbol{X} \quad \boldsymbol{X}_p$. The pressure and the velocity are continuous and linear, but we allow jumps in their slopes, that is, their slopes are piecewise constant. Let $\boldsymbol{N}$ denote the unit normal to the interface between cells c and d, see Fig. 9. In what follows, we omit the superscript n related to time in order to simplify the notations. We assume that $\boldsymbol{U}$, P and their derivatives are continuous across the characteristics in the direction $\boldsymbol{N}$ associated with the acoustic waves. The time derivatives are defined by setting

$$\left(\frac{d\boldsymbol{U}}{dt}\right)_p \quad \lim_{t \to t^n} \frac{d\boldsymbol{U}}{dt} \boldsymbol{X}_p, t \, , \tag{53a}$$

$$\left(\frac{d\Pi}{dt}\right)_{\overline{p}}^c \quad \lim_{t \to t^n} \lim_{\eta \to 0} \frac{dP}{dt} \boldsymbol{X}_p \quad \eta\boldsymbol{N}, t \, , \tag{53b}$$

$$\left(\frac{d\Pi}{dt}\right)_{\underline{p}}^d \quad \lim_{t \to t^n} \lim_{\eta \to 0} \frac{dP}{dt} \boldsymbol{X}_p \quad \eta\boldsymbol{N}, t \, , \tag{53c}$$

where $\eta > 0$. In the vicinity of $\boldsymbol{X}_p$ and for $t \to t^n$, the continuity of the derivative of P, $\frac{dP}{dt} \quad a\nabla P \cdot \boldsymbol{N}$ (resp. $\frac{dP}{dt} \quad a\nabla P \cdot \boldsymbol{N}$), across the characteristic in the direction $\boldsymbol{N}$ associated with the eigenvalue a (resp. a), leads to

$$\left(\frac{d\Pi}{dt}\right)_{\overline{p}}^c \quad a_c \ \nabla P_{\ \underline{p}}^{\ c} \cdot \boldsymbol{N} \quad \left(\frac{dP}{dt}\right)_c \quad a_c \ \nabla P_{\ c} \cdot \boldsymbol{N}, \tag{54a}$$

$$\left(\frac{d\Pi}{dt}\right)_{\underline{p}}^d \quad a_d \ \nabla P_{\ \underline{p}}^{\ d} \cdot \boldsymbol{N} \quad \left(\frac{dP}{dt}\right)_d \quad a_d \ \nabla P_{\ d} \cdot \boldsymbol{N}. \tag{54b}$$

Here, we have expressed the derivatives in two ways, approaching the characteristic from either side. We notice that we have kept the two-sided notation (such as a_c, a_d which are equal) in the previous equations so that we can use them in the numerical applications even for discontinuous states. Concerning the notations, we have set

$$\nabla P_{\ \overline{p}}^{\ c} \quad \lim_{t \to t^n} \lim_{\eta \to 0} \nabla P \boldsymbol{X}_p \quad \eta\boldsymbol{N}, t \, , \quad \nabla P_{\ \underline{p}}^{\ d} \quad \lim_{t \to t^n} \lim_{\eta \to 0} \nabla P \boldsymbol{X}_p \quad \eta\boldsymbol{N}, t \, .$$

The other notations are displayed in Fig. 10. With the help of Eq. (51b), we get

$$\nabla P_{\ \overline{p}}^{\ c} \quad \rho_c \left(\frac{d\boldsymbol{U}}{dt}\right)_p, \quad \nabla P_{\ \underline{p}}^{\ d} \quad \rho_d \left(\frac{d\boldsymbol{U}}{dt}\right)_p.$$
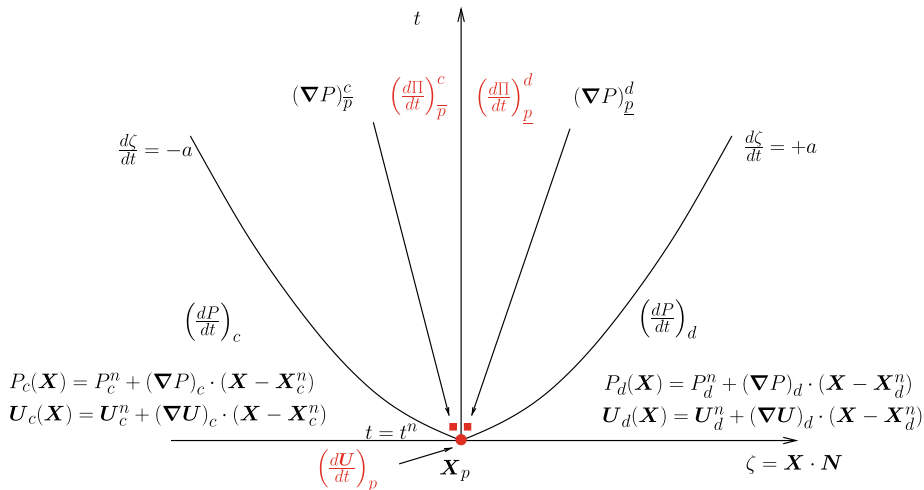

Fig. 10. Structure of the Generalized Riemann problem at point p in the direction of the unit normal $\boldsymbol{N}$. Note that $\zeta \quad \boldsymbol{X} \cdot \boldsymbol{N}$ is the variable in the direction of $\boldsymbol{N}$.

The time derivatives of pressure in the right-hand side of (54) are expressed thanks to Eq. (51a) and we finally obtain

$$\left(\frac{d\Pi}{dt}\right)^c_{\underline{p}} = Z_c\left(\frac{d\boldsymbol{U}}{dt}\right)_p \cdot \boldsymbol{N} + a_c\left[\nabla P_c \cdot \boldsymbol{N} - Z_c \nabla \cdot \boldsymbol{U}_c\right], \tag{55a}$$

$$\left(\frac{d\Pi}{dt}\right)^d_{\underline{p}} = Z_d\left(\frac{d\boldsymbol{U}}{dt}\right)_p \cdot \boldsymbol{N} + a_d\left[\nabla P_d \cdot \boldsymbol{N} - Z_d \nabla \cdot \boldsymbol{U}_d\right]. \tag{55b}$$

In the left-hand sides of the previous equations the pressure gradient is obtained using the piecewise linear reconstruction. Regarding the velocity divergence, it is computed taking the trace of the velocity gradient, that is $\nabla \cdot \boldsymbol{U}_c = \mathrm{Tr}\,\nabla \boldsymbol{U}_c$. Subtracting (55a) from (55b) we get

$$\left(\frac{d\Pi}{dt}\right)^d_{\underline{p}} - \left(\frac{d\Pi}{dt}\right)^c_{\underline{p}} = (Z_c + Z_d)\left[\left(\frac{d\boldsymbol{U}}{dt}\right)_p \cdot \boldsymbol{N} - \dot{\mathcal{V}}^\star_{c,d}\right],$$

where $\dot{\mathcal{V}}^\star_{c,d}$ is defined as follows

$$\dot{\mathcal{V}}^\star_{c,d} = \frac{a_c\left(\nabla P_c \cdot \boldsymbol{N} - Z_c \nabla \cdot \boldsymbol{U}_c\right) - a_d\left(\nabla P_d \cdot \boldsymbol{N} - Z_d \nabla \cdot \boldsymbol{U}_d\right)}{Z_c + Z_d}.$$

It turns out that $\dot{\mathcal{V}}^\star_{c,d}$ is the normal component of the one-dimensional solution of the acoustic GRP problem in the direction of the unit normal $\boldsymbol{N}$, refer to [23]. Therefore, the time derivatives of the nodal pressures are equal if and only if the projection of the time derivative of the node velocity onto the unit normal is equal to $\dot{\mathcal{V}}^\star_{c,d}$. Since in general $\left(\frac{d\boldsymbol{U}}{dt}\right)_p \cdot \boldsymbol{N} \neq \dot{\mathcal{V}}^\star_{c,d}$, we have the discontinuity $\left(\frac{d\Pi}{dt}\right)^c_{\underline{p}} \neq \left(\frac{d\Pi}{dt}\right)^d_{\underline{p}}$.

Finally, for each face, we introduce four time derivatives of the pressure, two for each node on each side of the edges. The discontinuity of these time derivatives across the face implies the loss of total energy conservation, on the contrary to the one-dimensional case. In what follows, we shall show how to compute these time derivatives by recovering total energy conservation.

We study total energy conservation writing the global balance of energy without taking into account the boundary conditions. The summation of the discrete total energy equation, refer to Step 3, over all the cells leads to

$$\sum_c m_c\left(E^{n+1}_c - E^n_c\right) = -\Delta t \sum_c \sum_{p\in\mathcal{P}_c}\left(\mathcal{R}^{c,n}_{\underline{p}}L^{c,n}_{\underline{p}}\Pi^{c,n}_{\underline{p}}\boldsymbol{N}^{c,n}_{\underline{p}} + \mathcal{R}^{c,n}_{\overline{p}}L^{c,n}_{\overline{p}}\Pi^{c,n}_{\overline{p}}\boldsymbol{N}^{c,n}_{\overline{p}}\right)\cdot\boldsymbol{U}^{n+\frac{1}{2}}_p$$

$$-\frac{\Delta t^2}{2}\sum_c\sum_{p\in\mathcal{P}_c}\left[\mathcal{R}^{c,n}_{\underline{p}}L^{c,n}_{\underline{p}}\left(\frac{d\Pi}{dt}\right)^{c,n}_{\underline{p}}\boldsymbol{N}^{c,n}_{\underline{p}} + \mathcal{R}^{c,n}_{\overline{p}}L^{c,n}_{\overline{p}}\left(\frac{d\Pi}{dt}\right)^{c,n}_{\overline{p}}\boldsymbol{N}^{c,n}_{\overline{p}}\right]\cdot\boldsymbol{U}^{n+\frac{1}{2}}_p$$

Here, we have expressed the nodal pressures $\Pi^{c,n+\frac{1}{2}}_{\underline{p}}, \Pi^{c,n+\frac{1}{2}}_{\overline{p}}$ thanks to the Taylor expansions (49b) and (49c). Switching the summation over cells and the summation over nodes in the right-hand side of the previous equation, we get

$$\sum_c m_c\left(E^{n+1}_c - E^n_c\right) = -\Delta t \sum_p \sum_{c\in\mathcal{C}_p}\left(\mathcal{R}^{c,n}_{\underline{p}}L^{c,n}_{\underline{p}}\Pi^{c,n}_{\underline{p}}\boldsymbol{N}^{c,n}_{\underline{p}} + \mathcal{R}^{c,n}_{\overline{p}}L^{c,n}_{\overline{p}}\Pi^{c,n}_{\overline{p}}\boldsymbol{N}^{c,n}_{\overline{p}}\right)\cdot\boldsymbol{U}^{n+\frac{1}{2}}_p$$

$$-\frac{\Delta t^2}{2}\sum_p\sum_{c\in\mathcal{C}_p}\left[\mathcal{R}^{c,n}_{\underline{p}}L^{c,n}_{\underline{p}}\left(\frac{d\Pi}{dt}\right)^{c,n}_{\underline{p}}\boldsymbol{N}^{c,n}_{\underline{p}} + \mathcal{R}^{c,n}_{\overline{p}}L^{c,n}_{\overline{p}}\left(\frac{d\Pi}{dt}\right)^{c,n}_{\overline{p}}\boldsymbol{N}^{c,n}_{\overline{p}}\right]\cdot\boldsymbol{U}^{n+\frac{1}{2}}_p$$

By construction of the nodal solver, the term between parentheses in the right-hand side cancels. Then, total energy conservation at the discrete level is ensured, provided that the term between brackets in the right-hand side cancels. Therefore, we deduce the following sufficient condition to ensure discrete total energy conservation

$$\sum_{c\in\mathcal{C}_p}\left[\mathcal{R}^{c,n}_{\underline{p}}L^{c,n}_{\underline{p}}\left(\frac{d\Pi}{dt}\right)^{c,n}_{\underline{p}}\boldsymbol{N}^{c,n}_{\underline{p}} + \mathcal{R}^{c,n}_{\overline{p}}L^{c,n}_{\overline{p}}\left(\frac{d\Pi}{dt}\right)^{c,n}_{\overline{p}}\boldsymbol{N}^{c,n}_{\overline{p}}\right] = \boldsymbol{0}. \tag{56}$$

We claim that this condition also implies the conservation of momentum for the control volume scheme, in the sense that the following balance is satisfied

$$\sum_c m_c\left(\boldsymbol{U}^{n+1}_c - \boldsymbol{U}^n_c\right) = \alpha\Delta t \sum_c A^{n+\frac{1}{2}}_c P^{n+\frac{1}{2}}_c \boldsymbol{e}_Y.$$

We note that condition (56) expresses the balance of the forces per unit time induced by the discontinuity of the time derivatives of the nodal pressures. The times derivatives of the nodal pressures, $\left(\frac{d\Pi}{dt}\right)^{c,n}_{\underline{p}}$ and $\left(\frac{d\Pi}{dt}\right)^{c,n}_{\overline{p}}$ are linked to the time derivative of the point velocity, $\left(\frac{d\boldsymbol{U}}{dt}\right)^n_p$, with the help of the following equations

$$\left(\frac{d\Pi}{dt}\right)^{c,n}_{\underline{p}} = Z^n_c\left(\frac{d\boldsymbol{U}}{dt}\right)^n_p \cdot \boldsymbol{N}^{c,n}_{\underline{p}} + a^n_c\left[\nabla P_c \cdot \boldsymbol{N}^{c,n}_{\underline{p}} - Z^n_c \nabla \cdot \boldsymbol{U}_c\right], \tag{57a}$$

$$\left(\frac{d\Pi}{dt}\right)^{c,n}_{\overline{p}} = Z^n_c\left(\frac{d\boldsymbol{U}}{dt}\right)^n_p \cdot \boldsymbol{N}^{c,n}_{\overline{p}} + a^n_c\left[\nabla P_c \cdot \boldsymbol{N}^{c,n}_{\overline{p}} - Z^n_c \nabla \cdot \boldsymbol{U}_c\right]. \tag{57b}$$

These equations are obtained writing the continuity of the derivatives of P, $\frac{dP}{dt} \quad a\nabla P \cdot \mathbf{N}_{\underline{p}}^{c,n}$ and $\frac{dP}{dt} \quad a\nabla P \cdot \mathbf{N}_{\overline{p}}^{c,n}$, across the characteristics in the directions $\mathbf{N}_{\underline{p}}^{c,n}$ and $\mathbf{N}_{\overline{p}}^{c,n}$ associated with the eigenvalue a. Once more, this is done in the vicinity of $\mathbf{X}_p$ and for $t \to t^n$ (refer to Fig. 11). It turns out that the combination of (56) and (57) written for each cell surrounding point p, constitutes a closed set of equations that allows to determine the time derivatives. Substituting Eqs. (57a) and (57b) into the sufficient condition (56), one obtains

$$
\mathsf{G}_p \left(\frac{d\mathbf{U}}{dt}\right)^n_p \quad \sum_{c \in \mathcal{C}_p} a_c^n \Big[\mathsf{G}_p^c \quad P_c \quad Z_c^n \Big(\mathcal{R}_{\underline{p}}^{c,n} L_{\underline{p}}^{c,n} \mathbf{N}_{\underline{p}}^{c,n} \quad \mathcal{R}_{\overline{p}}^{c,n} L_{\overline{p}}^{c,n} \mathbf{N}_{\overline{p}}^{c,n}\Big) \quad \cdot \mathbf{U}_c\Big],
$$

where G_p^c and G_p are the 2×2 matrices defined by

$$
\mathsf{G}_p^c \quad Z_c^n \Big[\mathcal{R}_{\underline{p}}^{c,n} L_{\underline{p}}^{c,n} \; \mathbf{N}_{\underline{p}}^{c,n} \otimes \mathbf{N}_{\underline{p}}^{c,n} \quad \mathcal{R}_{\overline{p}}^{c,n} L_{\overline{p}}^{c,n} \; \mathbf{N}_{\overline{p}}^{c,n} \otimes \mathbf{N}_{\overline{p}}^{c,n}\Big], \quad \mathsf{G}_p \quad \sum_{c \in \mathcal{C}_p} \mathsf{G}_p^c.
$$

We note that these matrices coincide with the matrices M_p and M_p^c introduced in the nodal solver in the case of the acoustic approximation. Matrices G_p^c and G_p are symmetric positive definite, thus G_p is always invertible and the time derivative of the point velocity is written

$$
\left(\frac{d\mathbf{U}}{dt}\right)^n_p \quad \mathsf{G}_p^1 \sum_{c \in \mathcal{C}_p} a_c^n \Big[\mathsf{G}_p^c \quad P_c \quad Z_c^n \Big(\mathcal{R}_{\underline{p}}^{c,n} L_{\underline{p}}^{c,n} \mathbf{N}_{\underline{p}}^{c,n} \quad \mathcal{R}_{\overline{p}}^{c,n} L_{\overline{p}}^{c,n} \mathbf{N}_{\overline{p}}^{c,n}\Big) \quad \cdot \mathbf{U}_c\Big]. \tag{58}
$$

The time derivatives of the nodal pressures are deduced from (57).

Finally, we have constructed a nodal solver to compute the time derivatives of the node-based fluxes. This solver can be viewed as the two-dimensional extension of the one-dimensional acoustic GRP solver derived by Ben-Artzi and Falcovitz. We note that this nodal solver can handle both control volume and area weighted formulations. Moreover, it ensures rigorously total energy conservation at the discrete level.

Comment 6. A closer inspection of the formulae (58) and (57) reveals that by setting the slopes to zero in the piecewise linear reconstruction, the time derivatives of the node-based fluxes cancel out. Hence, our algorithm recovers naturally the first-order scheme.

4.2.3. Computation of the time derivative of the cell pressure

For the control volume scheme, we need to compute the time derivative of the cell pressure, $\left(\frac{dP}{dt}\right)^n_c$. This computation is easily performed using Eq. (51a) and we finally obtain

$$
\left(\frac{dP}{dt}\right)^n_c \quad \rho_c a_c^2 \quad \cdot \mathbf{U}_c,
$$

where the divergence of the velocity is obtained through the use of the piecewise linear reconstruction.

5. Time step control

For numerical applications, the time step is evaluated following two criteria. The first one is a standard CFL criterion which heuristically guarantees the monotone behavior of the entropy. The second is more intuitive, but reveals very useful in practice: we limit the variation of the volume of cells over one time step.
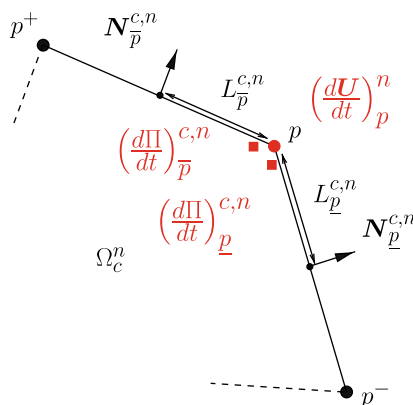

Fig. 11. Localization of the time derivatives of the nodal pressures and velocity at point p viewed from cell Ω_c^n.

5.1. CFL like criterion

We propose a CFL like criterion in order to ensure a positive entropy production in cell Ω_c during the time step. At time t_n, for each cell Ω_c we denote by L_c^n the minimal value of the distance between two points of the cell. We define

$$\Delta t_E = C_E \min_c \frac{L_c^n}{a_c^n},$$

where C_E is a strictly positive coefficient and a_c is the sound speed in the cell. The coefficient C_E is computed heuristically and we provide no rigorous analysis which allows such formula. However, extensive numerical experiments show that $C_E = 0.25$ is a value which provides stable numerical results. We have also checked that this value is compatible with a monotone behavior of entropy. The rigorous derivation of this criterion could be obtained by computing the time step which ensures a positive entropy production in cell Ω_c from time t^n to t^{n+1}.

5.2. Criterion on the variation of volume

We require that a cell does not change its volume by too large an amount in a time step. We estimate the volume of the cell Ω_c at $t = t^{n+1}$ through the use of the Taylor expansion

$$V_c^{n+1} = V_c^n + \frac{d}{dt} V_c (t^n) \Delta t.$$

Here, the time derivative $\frac{d}{dt} V_c$ is computed using the discrete GCL. Let C_V be a strictly positive coefficient, $C_V \in]0,1[$. We look for Δt such that

$$\frac{V_c^{n+1} - V_c^n}{V_c^n} \leqslant C_V.$$

To do so, we define

$$\Delta t_V = C_V \min_c \left\{ \frac{V_c^n}{\frac{d}{dt} V_c (t^n)} \right\}.$$

For numerical applications, we choose $C_V = 0.1$.

Last, the estimation of the next time step Δt^{n+1} is given by

$$\Delta t^{n+1} = \min \left(\Delta t_E, \Delta t_V, C_M \Delta t^n \right), \tag{59}$$

where Δt^n is the current time step and C_M is a multiplicative coefficient which allows the time step to increase. We generally set $C_M = 1.01$.

6. Numerical results

In this section, we present several test cases to assess the robustness of the control volume and the area-weighted schemes. For each problem, we use a perfect gas equation of state which is taken to be of the form $P = (\gamma - 1) \rho \varepsilon$, where γ is the polytropic index. The computations have been made using the Dukowicz approximation for the nodal solver [16], namely the coefficient Γ_c in the mass swept flux is set equal to $\frac{\gamma+1}{2}$.

6.1. Spherical Sod problem

Here, we consider the extension of the classical Sod shock tube [32] to the case of spherical geometry. The present problem consists of a spherical shock tube of unity radius. The interface is located at $r = 0.5$. At the initial time, the states on the left and on the right sides of the interface are constant. The left state is a high pressure fluid characterized by $(\rho_L, P_L, u_L) = (1, 1, 0)$, the right state is a low pressure fluid defined by $(\rho_R, P_R, u_R) = (0.125, 0.1, 0)$. The gamma gas law is defined by $\gamma = \frac{7}{5}$. The computational domain is defined in polar coordinates by $(r, \theta) \in [0,1] \times [0, \frac{\Pi}{2}]$ where $r = \sqrt{x^2 + y^2}$ and $\theta = \arctan \left(\frac{y}{x} \right)$. The initial grid is a polar grid with 100×9 equally spaced zones both in the radial and angular direction. The boundary conditions are wall boundary conditions, that is, the normal velocity is set to zero at each boundary.

The aim of this test case is to assess the symmetry preservation ability for the area-weighted and control volume schemes. In what follows, we define a numerical indicator that measures the loss of symmetry preservation. The polar grid is described using logical j-lines radially outward and logical i-lines in the angular direction. For the logical i-line, let us introduce the averaged radius

$$\overline{R}_i = \frac{1}{J+1} \sum_{j=1}^{J+1} R_{i,j},$$

where J 1 denotes the number of logical j-lines and $R_{i,j}$ is the radius of the node located at the intersection of the logical i-lines and the logical j-line. Then, we define the difference between the averaged radius and the generic radius along the logical i-line

$$\Delta R_i \quad \max_{j \ 1, \dots, J \ 1} R_{i,j} \quad \overline{R}_i .$$

Finally, we introduce the global indicator which characterizes the symmetry preservation by setting

$$\Delta R \quad \max_{i \ 1, \dots, I \ 1} \Delta R_i,$$

where I 1 denotes the number of logical i-lines.

We run the Spherical Sod problem using the high-order area-weighted scheme and the first and high-order control volume scheme. The corresponding ΔR indicators are displayed in Fig. 12 as function of time, using a logarithmic scale.

We remark that symmetry preservation is ensured to numerical roundoff for the area-weighted scheme. As expected, the control volume scheme does not ensure symmetry preservation. However, it is interesting to note that the high-order extension performs better than the first-order version, as it can be seen in Fig. 13. This last result corroborates the theoretical study that has been performed in Section 3.7.3 concerning the symmetry preservation in the case of a one-dimensional spherical flow in cylindrical geometry.

We have also displayed in Fig. 14 the numerical density computed with the high-order area-weighted scheme as function of the cell center radius versus a reference solution. This reference solution has been computed using a one-dimensional second-order spherical Lagrangian code with 10,000 cells. We note the good agreement between the numerical and the reference solution. One can clearly see the non-oscillatory behavior of the proposed high-order scheme. We emphasize that in particular the beginning and the end of the rarefaction fan are difficult to capture and that especially here, our high-order scheme performs quite well.

6.2. Kidder's isentropic compression

In [20], Kidder has analytically computed the solution of the self-similar isentropic compression of a shell filled with perfect gas. This analytical solution is particularly useful in order to assess the ability of a Lagrangian scheme to properly compute a spherical isentropic compression. More precisely, we want to check that the area-weighted scheme does not produce spurious entropy during the isentropic compression.

We briefly recall the main features of this solution in order to define the test case. Initially, the shell has the internal (resp. external) radius r_b (resp. r_e). Let P_b, P_e, ρ_b, and ρ_e be the pressures and densities located at r_b and r_e. Since the compression is isentropic, we define $s \quad \frac{P_e}{\rho^\gamma_e}$, and we have $\rho_b \quad \rho_e \left(\frac{P_b}{P_e}\right)^{\frac{1}{\gamma}}$. Let $R \ r, t$ be the radius at time $t > 0$ of a fluid particle initially located at radius r. Looking for a solution of the gas dynamics equation under the form $R \ r, t \quad h \ t \ r$, using the isentropic fea-
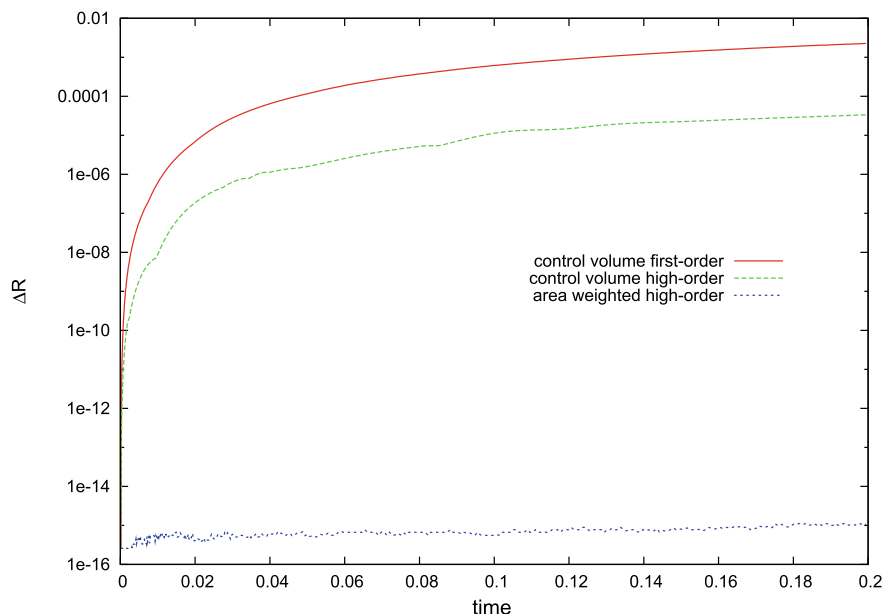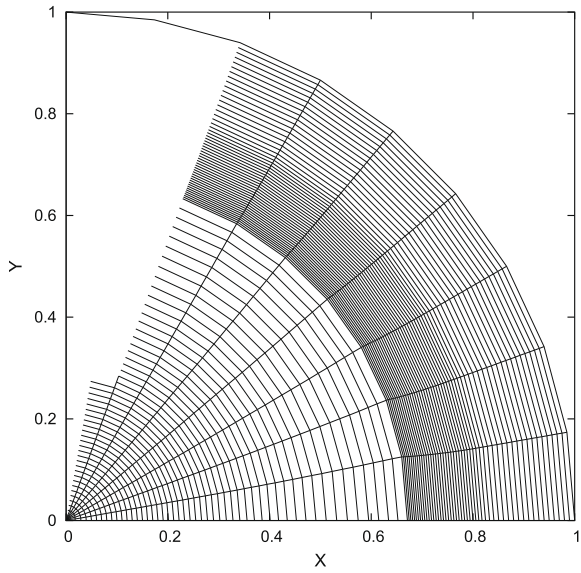

Fig. 12. Symmetry preservation indicator as function of time for the spherical Sod problem.

ture of the flow and setting $\gamma = 1 + \frac{2}{\nu}$, where $\nu = 1, 2, 3$ indicates planar, cylindrical or spherical symmetry, we finally get the self-similar analytical solution for $t \in [0, \tau]$

$$\rho(R(r,t), t) = [h(t)]^{-\frac{2}{\gamma-1}} \rho_0 \left[\frac{R(r,t)}{h(t)} \right],$$

$$u(R(r,t), t) = \frac{d}{dt} h(t) \frac{R(r,t)}{h(t)},$$

$$P(R(r,t), t) = [h(t)]^{-\frac{2\gamma}{\gamma-1}} P_0 \left[\frac{R(r,t)}{h(t)} \right].$$

Here, τ denotes the focusing time of the shell which is written

$$\tau = \sqrt{\frac{\gamma - 1}{2}\left(\frac{r_e^2}{a_e^2} - \frac{r_b^2}{a_b^2}\right)},$$

where $a^2 = s\gamma\rho^{\gamma-1}$ is the square of the isentropic sound speed. The particular form of the polytropic index enables us to get the analytical expression $h(t) = \sqrt{1 - \left(\frac{t}{\tau}\right)^2}$, which is valid for any $t \in [0, \tau]$. Note that $h(t)$ goes to zero when t goes to τ, hence τ corresponds to the collapse of the shell on itself. For $r \in [r_b, r_e]$, the initial density and pressure, ρ_0, P_0, are defined by

$$\rho^0(r) = \left(\frac{r_e^2 - r^2}{r_e^2 - r_b^2}\rho_b^{\gamma-1} + \frac{r^2 - r_b^2}{r_e^2 - r_b^2}\rho_e^{\gamma-1}\right)^{\frac{1}{\gamma-1}},$$
$$P^0(r) = s\,\rho^0(r)^\gamma.$$

Note that the initial velocity is equal to zero since the shell is assumed to be initially at rest. The isentropic compression is obtained imposing the following pressure laws at the internal and external faces of the shell:

$$P(R(r_b, t), t) = P_b h(t)^{-\frac{2\gamma}{\gamma-1}},$$
$$P(R(r_e, t), t) = P_e h(t)^{-\frac{2\gamma}{\gamma-1}}.$$

We point out that the velocity field is a linear function of the radius R which is a typical property of self-similar isentropic compression.

For numerical applications, we consider the spherical shell characterized by $r_b = 0.9$ and $r_e = 1$. We set $P_b = 0.1$, $P_e = 10$, and $\rho_e = 10^{-2}$. Due to spherical symmetry we have $v = 3$, hence $\gamma = \frac{5}{3}$. The previous values lead to $\rho_b = 6.31 \times 10^{-4}$, $s = 2.15 \times 10^4$ and, $\tau = 6.72 \times 10^{-3}$.

The initial computational domain is defined in polar coordinates by $(r, \theta) \in [0.9, 1] \times [0, \frac{\pi}{6}]$, where $r = \sqrt{x^2 + y^2}$ and $\theta = \arctan\frac{y}{x}$. The computational domain is paved using equally spaced zones in the radial and the angular directions. Kidder's problem is run with the three following polar grids: 25×15, 50×30 and 100×60. The stopping time is chosen to be very close to the focusing time setting $t_s = 0.99\tau$. The computations are performed with the high-order scheme using the Barth–Jespersen limiter. To precisely estimate the entropy production we define the entropy parameter

$$\alpha = \frac{P}{s\rho^\gamma}.$$

We note that for a perfect isentropic compression α is equal to one.

We have plotted in Fig. 15 the radial component of the velocity versus the analytical solution at the stopping time. We note that the linear feature of the velocity is very well preserved. We can also see the convergence of the numerical solutions toward the analytical one. In order to evaluate the entropy production, we have displayed in Fig. 16 the entropy parameter for the high-order GRP scheme. It turns out that the high-order GRP extension dramatically decreases the value of the en-
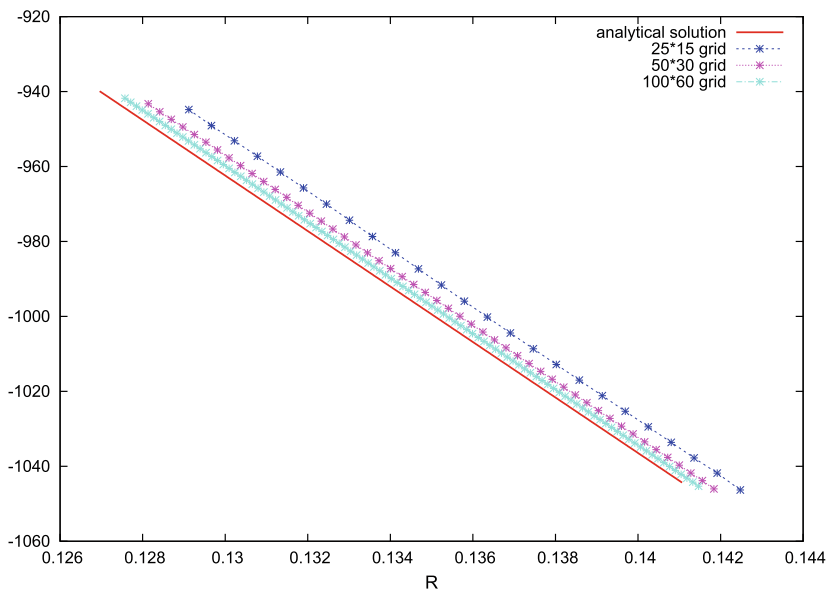

Fig. 15. Kidder's isentropic compression. Radial component of the velocity as function of radius versus analytical solution at stopping time $t_s = 0.99\tau$.
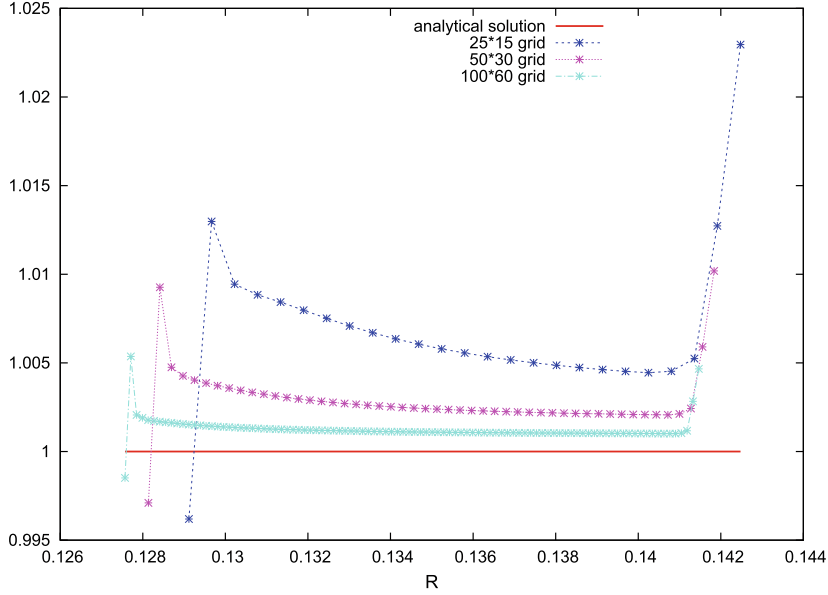
Fig. 16. Kidder's isentropic compression. Entropy parameter as a function of radius versus analytical solution at stopping time $t_s = 0.99\tau$.

tropy parameter and reaches the analytical value. Therefore, we can conclude that our GRP high-order area-weighted scheme is able to compute properly isentropic compressions.
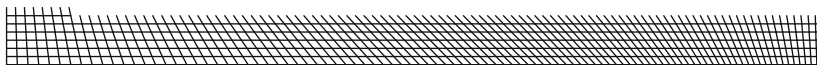
6.3. Saltzman problem

This test case taken from [17] is a well known difficult problem that evaluates the robustness of Lagrangian schemes. It consists of a strong piston-driven shock wave calculated using an initially nonuniform mesh. The computational domain is defined by $(x, y) \in [0, 1] \times [0, 0.1]$. The skewed initial mesh, displayed in Fig. 17, is obtained transforming a uniform 100×10 Cartesian grid with the mapping

$$x_{sk} = x + (0.1 - y) \sin(\pi x),$$
$$y_{sk} = y.$$

The initial conditions are $(\rho_0, \varepsilon_0, \boldsymbol{U}_0) = (1, 10^{-6}, \boldsymbol{0})$ and the polytropic index is $\gamma = \frac{5}{3}$. At $x = 0$, a unit inward normal velocity is prescribed, the other boundary conditions are reflective ones. The analytical solution is a one-dimensional infinite strength shock wave that moves at speed $D = \frac{4}{3}$ in the right direction. Thus, the shock wave hits the face $x = 1$ at time $t = 0.75$. Behind the shock, the density is equal to 4. Fig. 18 shows the grid and the density in all the cells as a function of cell-center X coordinate at $t = 0.8$ after the shock has hit the fixed wall at $X = 1$ and has bounced part way back toward the moving piston. The area-weighted scheme has been used; the density should be 4 and 10 in the two regions and is close to these values. We also notice the good agreement of the shock position with its analytical value $X_{shock} = \frac{29}{30} \approx 0.967$. In Fig. 19, the same plots are displayed using the control volume scheme. The discrepancies between the results obtained using both schemes are quite important and essentially localized in the shock plateau region.
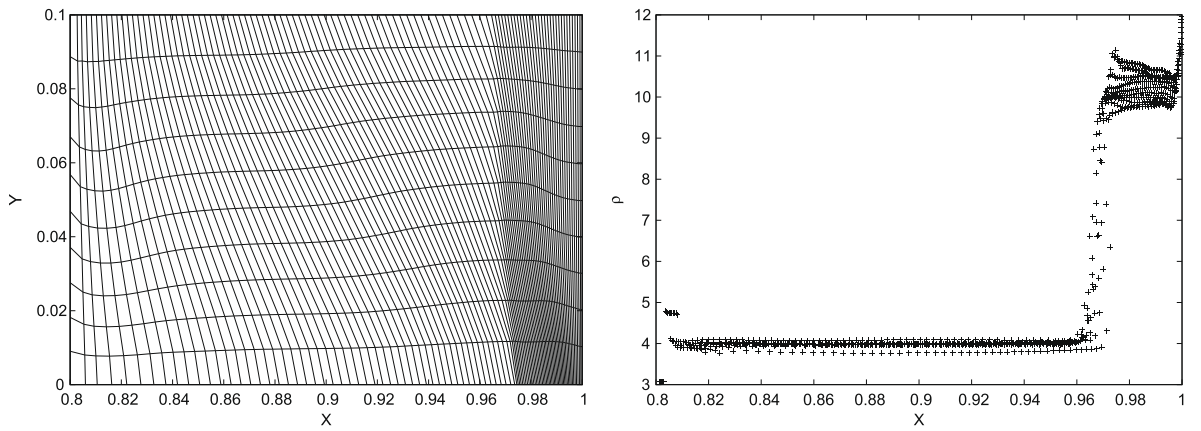
6.4. Sedov problem

We consider the Sedov problem for a point-blast in a uniform medium with spherical symmetry. An exact solution based on self-similarity arguments is available, see for instance [19]. The initial conditions are characterized by $(\rho_0, P_0, \boldsymbol{U}_0) = (1, 10^{-6}, \boldsymbol{0})$ and the polytropic index is set equal to $\frac{7}{5}$. We set an initial delta-function energy source at the origin prescribing the pressure in the cell containing the origin as follows
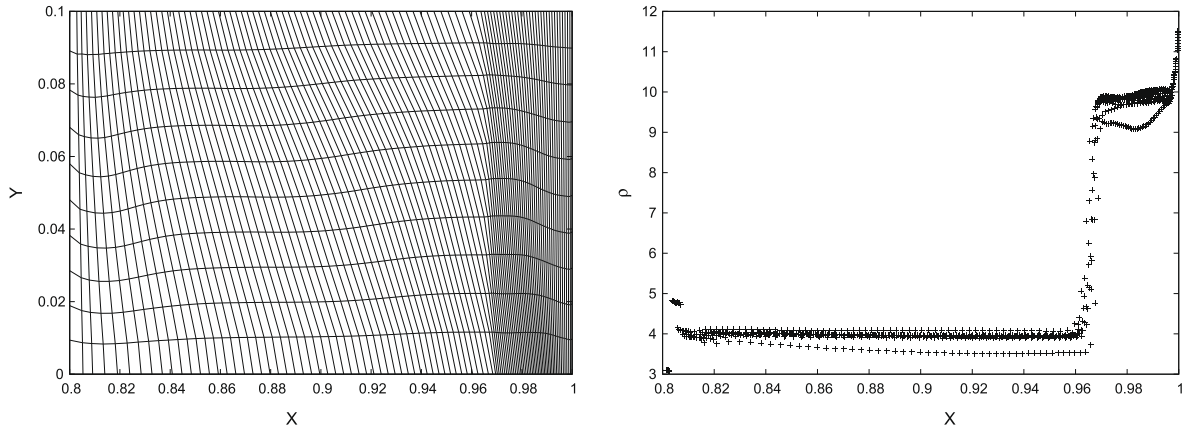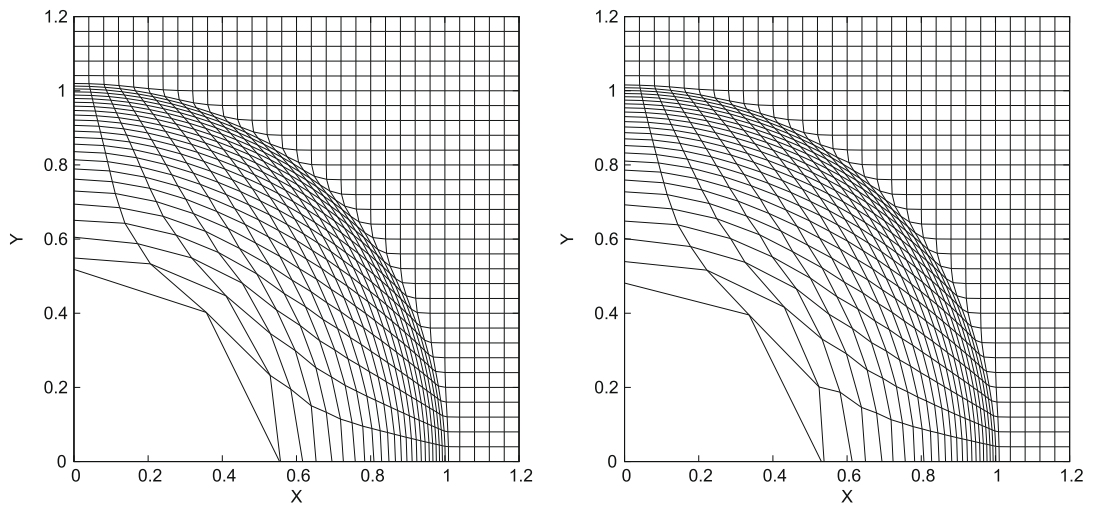
Fig. 18. Saltzman piston problem for the area-weighted scheme at time t 0.8. Grid (left). Density in all the cells as a function of cell-center X coordinate (right).

Fig. 19. Saltzman piston problem for the control volume scheme at time t 0.8. Grid (left). Density in all the cells as a function of cell-center X coordinate (right).

Fig. 20. Grid at the stopping time for the Sedov problem run with the Cartesian grid. Area-weighted scheme (left) and control volume scheme (right).

$$P_{\text{or}} = \left(\gamma - 1 \right) \rho_{\text{or}} \frac{\mathcal{E}_0}{V_{\text{or}}},$$

where V_{or} denotes the volume of the cell and $\mathcal{E}_0$ is the total amount of released energy. Choosing $\mathcal{E}_0 = 0.425536$, as it is suggested in [19], the solution consists of a diverging shock whose front is located at radius $R = 1$ at time $t = 1$. The peak density reaches the value 6.

First, we run a computation using a square grid with an edge of length 1.2 divided into 30×30 square zones. Then, keeping the same conditions, we run the Sedov problem on a polygonal grid produced by a Voronoi tessellation [22]. For each grid we use successively the control volume scheme and the area-weighted scheme with their high-order extension.

The final mesh for both schemes corresponding to the Cartesian grid are displayed in Fig. 20. The results are quite similar for both formulation. We note that the spherical shape of the shock wave is quite well preserved. As it can be seen in Fig. 21 the shock location is very well resolved without any spurious oscillations. The peak density reached by the numerical solution is in good agreement with the theoretical value. Similar results corresponding to the polygonal grid are presented in
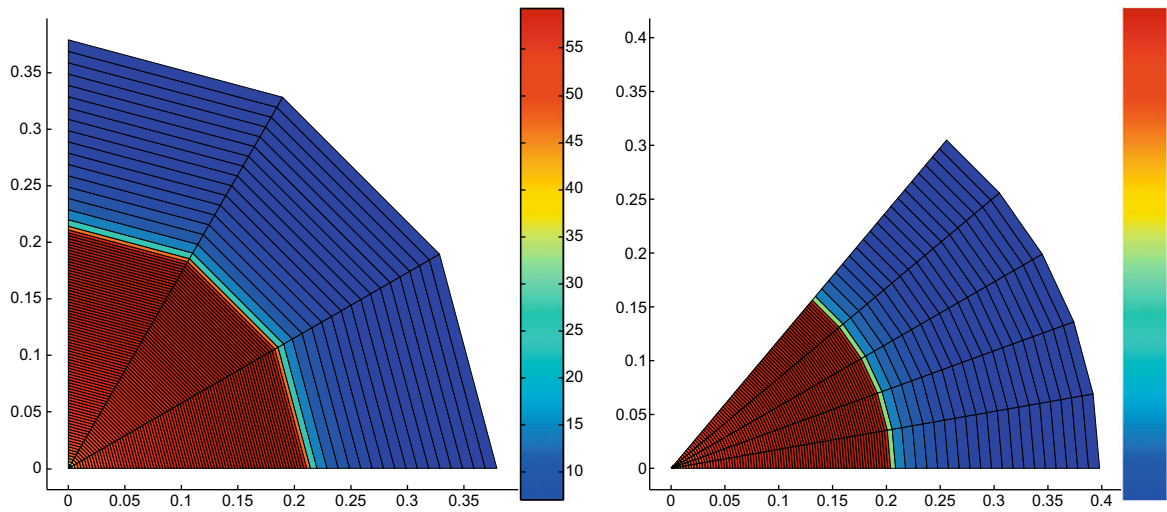
Figs. 22 and 23. Once more, we note the spherical shape of the shock wave and the good agreement with the analytical solution. These last results reveal the ability of our high-order Lagrangian scheme to handle unstructured grids.

6.5. Noh problem

The Noh problem [30] is a well known test problem that has been used extensively to validate Lagrangian scheme in the regime of strong shock waves. In this test case, a cold gas with unit density is given an initial inward radial velocity of magnitude 1. Then, a diverging spherical shock wave is generated which propagates at speed $D = \frac{1}{3}$. The density plateau behind the shock wave reaches the value 64. In order to demonstrate the robustness and the accuracy of our GRP area-weighted scheme, we shall run this test using polar grids with equi-angular zoning. The initial computational domain is defined in polar coordinates by $r, \theta \in [0, 1] \times [0, \frac{\pi}{2}]$.

First, we address the problem of wave front invariance. This requirement which has been introduced in [10] in the framework of staggered schemes, points out that the artificial viscosity should have no effect along a wave front of constant phase.
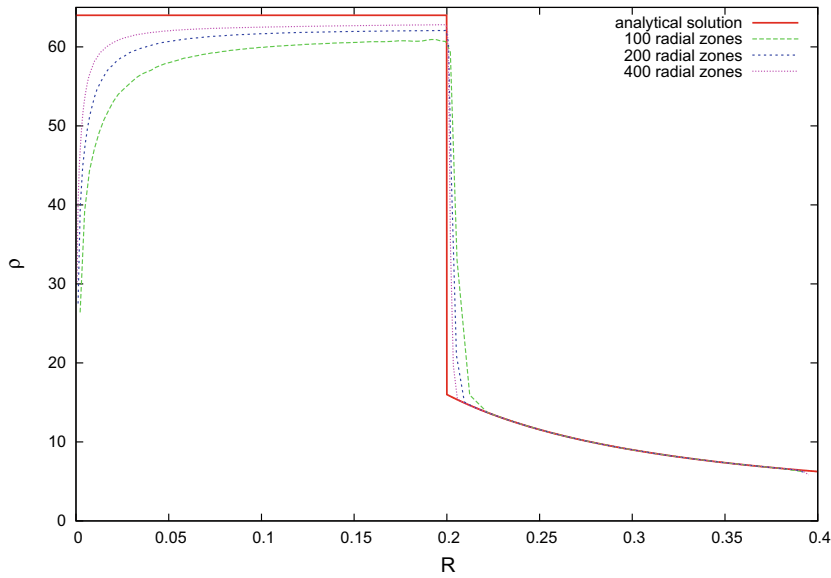

Fig. 26. Density as a function of radius for the Noh problem at stopping time $t = 0.6$. Convergence analysis.
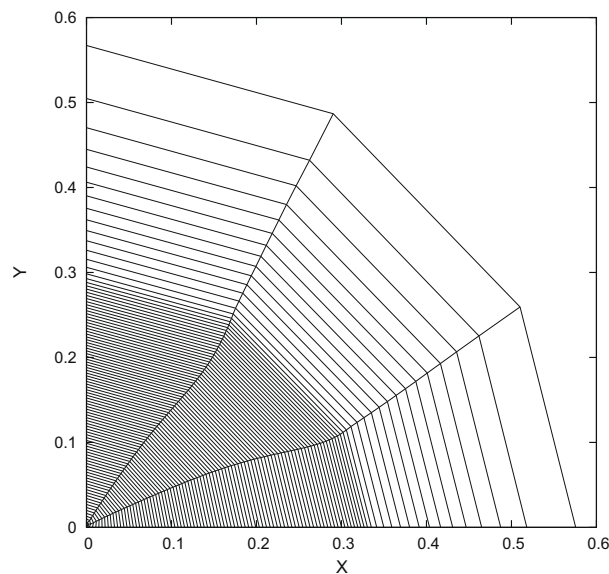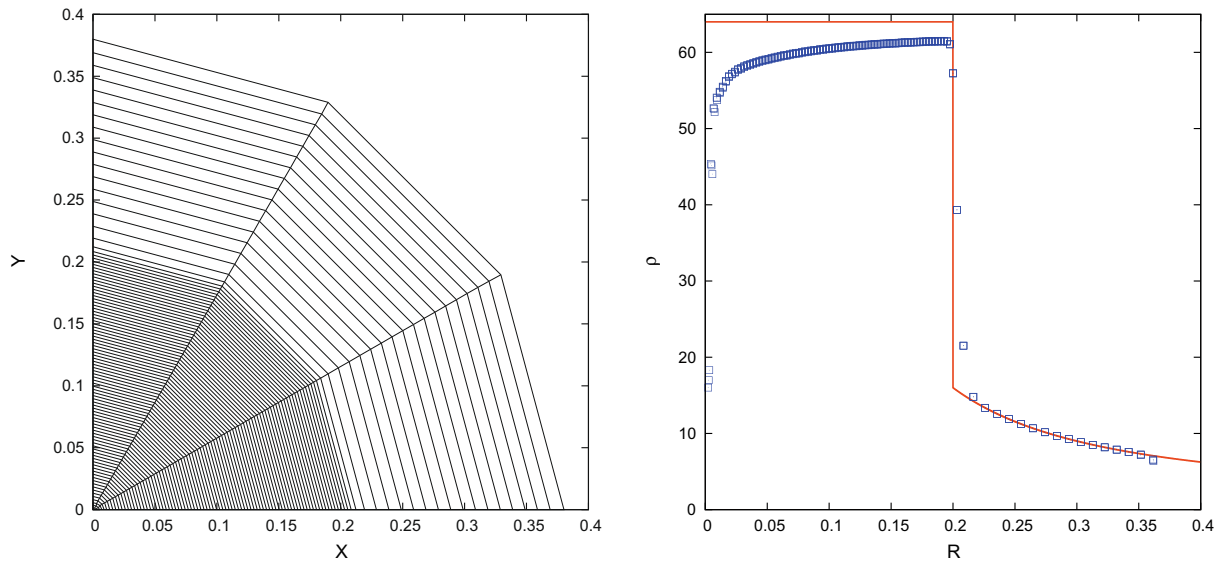

Fig. 27. Noh problem: grid at the stopping time using the first-order control volume scheme.

Fig. 28. Noh problem: grid at the stopping time (left) and density as a function of cell center radii (right) obtained using the high-order control volume scheme.

In the case of our cell-centered scheme, there is no artificial viscosity, however we have to check that the numerical viscosity inherent to our scheme satisfies this wave front invariance requirement. To examine this, we run the Noh problem with two polar grids characterized by the same zoning in the radial direction and two different angular zonings. The density maps at the stopping time t　0.6 are displayed in Fig. 24. We note that the symmetry is perfectly preserved. The shock location and the shock plateau agree quite well with the analytical solution. In Fig. 25, we have plotted the density as a function of radius for these two different angular zonings. The small difference between the two curves shows that the wave front invariance requirement is quite well satisfied. Finally, we assess the convergence of our scheme computing the Noh problem with the three following polar grids: 100×9, 200×9 and 400×9. We can observe in Fig. 26 the convergence of the numerical solutions toward the analytical one.

To assess the robustness and the accuracy of our control volume formulation, we have run the Noh problem using an equi-angular 100×3 polar grid, knowing that this scheme does not preserve symmetry. The final grid for the first-order control volume scheme is displayed in Fig. 27. We note the severe distortion of the grid due to the loss of symmetry of the scheme. The grid at the stopping time and the density as a function of cell center radii obtained using the high-order control volume scheme are shown in Fig. 28. We note the dramatic improvement induced by the high-order extension of the control volume scheme. Using this high-order extension, symmetry is not perfectly achieved, however the quality of the numerical result has been considerably enhanced. Once more, this result confirms the theoretical analysis performed in Section 3.7.3 concerning symmetry preservation.

7. Conclusion

We have described two cell-centered Lagrangian schemes for solving the compressible gas dynamics equations written in cylindrical geometry, using an unstructured mesh. The control volume scheme and the area-weighted scheme use a node-based discretization of the numerical fluxes that is compatible with the geometric conservation law. These two schemes only differ in the way the momentum equation has been discretized. The control volume scheme conserves momentum, total energy and satisfies a local entropy inequality in its first-order semi-discrete version. However, it does not preserve spherical symmetry. On the other hand, the area-weighted scheme preserves spherical symmetry for one-dimensional spherical flow on equi-angular polar grid. It also conserves total energy. In both formulations the node-based fluxes are computed thanks to a two-dimensional approximate Riemann solver. The high-order extension of both schemes is constructed using the generalized Riemann problem methodology in the acoustic framework. The numerical results demonstrated the accuracy and the robustness of these new schemes. In the future, we intend to investigate improvements related to the problem of symmetry preservation for spherical flows computed on polar grids.

Acknowledgments

References

[1] F.L. Adessio, D.E. Carroll, K.K. Dukowicz, J.N. Johnson, B.A. Kashiwa, M.E. Maltrud, H.M. Ruppel, Caveat: a computer code for fluid dynamics problems with large distortion and internal slip, Technical Report LA-10613-MS, Los Alamos National Laboratory, 1986.
[2] T.J. Barth, Numerical methods for conservation laws on structured and unstructured meshes, Technical Report, VKI Lecture Series, 2003.
[3] T.J. Barth, D.C. Jespersen, The design and application of upwind schemes on unstructured meshes, in: AIAA Paper 89-0366, 27th Aerospace Sciences Meeting, Reno, Nevada, 1989.
[4] M. Ben-Artzi, J. Falcovitz, A second-order Godunov-type scheme for compressible fluid dynamics, J. Comput. Phys. 55 (1) (1984) 1–32.
[5] M. Ben-Artzi, J. Falcovitz, An upwind second-order scheme for compressible duct flows, SIAM J. Sci. Stat. Comput. 7 (3) (1986) 744–768.
[6] M. Ben-Artzi, J. Falcovitz, Generalized Riemann Problems in Computational Fluids Dynamics, Cambridge University press, 2003.
[7] D.E. Burton, M. Shashkov, Exploration of some unconventional approaches to Lagrangian hydrodynamics, Technical Report LA-UR-07-7548, Los Alamos National Laboratory, 2007.
[8] J.C. Campbell, M.J. Shashkov, A tensor artificial viscosity using a mimetic finite difference algorithm, J. Comput. Phys. 172 (4) (2001) 739–765.
[9] J.C. Campbell, M.J. Shashkov, A compatible Lagrangian hydrodynamics algorithm for unstructured grids, Selçuk J. Appl. Math. 4 (2) (2003) 53–70.
[10] E.J. Caramana, M.J. Shashkov, P.P. Whalen, Formulations of artificial viscosity for multidimensional shock wave computations, J. Comput. Phys. 144 (1998) 70–97.
[11] E.J. Caramana, D.E. Burton, M.J. Shashkov, P.P. Whalen, The construction of compatible hydrodynamics algorithms utilizing conservation of total energy, J. Comput. Phys. 146 (1998) 227–262.
[12] E.J. Caramana, M.J. Shashkov, Elimination of artificial grid distortion and hourglass-type motions by means of Lagrangian subzonal masses and pressures, J. Comput. Phys. 142 (1998) 521–561.
[13] E.J. Caramana, P. P Whalen, Numerical preservation of symmetry properties of continuum problems, J. Comput. Phys. 141 (1998) 174–198.
[14] S.R. de Groot, P. Mazur, Non-equilibrium Thermodynamics, Dover, 1984.
[15] B. DesprTs, C. Mazeran, Lagrangian gas dynamics in two dimensions and Lagrangian systems, Arch. Rational Mech. Anal. 178 (2005) 327–372.
[16] J.K. Dukowicz, A general non-iterative Riemann solver for Godunov's method, J. Comput. Phys. 61 (1984) 119–137.
[17] J.K. Dukowicz, B. Meltz, Vorticity errors in multidimensional Lagrangian codes, J. Comput. Phys. 99 (1992) 115–134.
[18] E. Godlewski, P.-A. Raviart, Hyperbolic Systems of Conservation Laws, Springer-Verlag, 2000.
[19] J.R. Kamm, F.X. Timmes, On efficient generation of numerically robust Sedov solutions, Technical Report LA-UR-07-2849, Los Alamos National Laboratory, 2007.
[20] R.E. Kidder, Laser-driven compression of hollow shells: power requirements and stability limitations, Nucl. Fusion 1 (1976) 3–14.
[21] J. Li, Z. Sun, Remark on the generalized Riemann problem method for compressible fluid flows, J. Comput. Phys. 222 (2007) 796–808.
[22] R. Loubère, M.J. Shashkov, A subcell remapping method on staggered polygonal grids for Arbitrary-Lagrangian–Eulerian methods, J. Comput. Phys. 209 (2005) 105–138.
[23] P.-H. Maire, A high-order cell-centered Lagrangian scheme for two-dimensional compressible fluid flows on unstructured meshes, J. Comput. Phys. 228 (2009) 2391–2425.
[24] P.-H. Maire, R. Abgrall, J. Breil, J. Ovadia, A cell-centered Lagrangian scheme for compressible flow problems, SIAM J. Sci. Comput. 29 (4) (2007) 1781–1824.
[25] P.-H. Maire, B. Nkonga, Multi-scale Godunov-type method for cell-centered discrete Lagrangian hydrodynamics, J. Comput. Phys. 228 (2009) 799–821.
[26] L. Margolin, M. Shashkov, P. Smolarkiewicz, A discrete operator calculus for finite difference approximations, Comput. Methods Appl. Mech. Eng. 187 (2000) 365–383.
[27] L.G. Margolin, M.J. Shashkov, Using a curvilinear grid to construct symmetry-preserving discretizations for Lagrangian gas dynamics, J. Comput. Phys. 149 (1999) 389–417.
[28] L.G. Margolin, M.J. Shashkov, M.A. Taylor, Symmetry-preserving discretizations for Lagrangian gas dynamics, in: P. NeittaanmSki, T. Tiihonen, P. Tarvainen (Eds.), Proceedings of the Third European Conference Numerical Mathematics and Advanced Applications, World Scientific, 2000, pp. 725–732.
[29] C. Mazeran, Sur la structure mathématique et l'approximation numérique de l'hydrodynamique Lagrangienne bidimensionelle, PhD Thesis, Université Bordeaux I, 2007.
[30] W.F. Noh, Errors for calculations of strong shocks using artificial viscosity and an artificial heat flux, J. Comput. Phys. 72 (1987) 78–120.
[31] Z.J. Shen, G.W. Yuan, J.Y. Yue, X.Z. Liu, A cell-centered Lagrangian scheme in two-dimensional cylindrical geometry, Sci. China Ser. A: Math. 51 (8) (2008) 1479–1494.
[32] G.A. Sod, A survey of several finite difference methods for systems of non-linear hyperbolic conservation laws, J. Comput. Phys. 27 (1978) 1–31.
[33] A.V. Solov'ev, M.Yu. Shashkov, Difference scheme for the Dirichlet particle method in cylindrical coordinates, conserving symmetry of gas-dynamical flow, Diff. Equat. 24 (7) (1988) 817–823.
[34] J. von Neumann, R.D. Richtmyer, A method for the numerical calculations of hydrodynamical shocks, J. Appl. Phys. 21 (1950) 232–238.
[35] P. Whalen, Algebraic limitations on two dimensional hydrodynamics simulations, J. Comput. Phys. 124 (1996) 46–54.
[36] M.L. Wilkins, Calculation of elastic plastic flow, Methods Comput. Phys. 3 (1964).